Norwegian University
of Life Sciences

Master's Thesis 2023 30 ECTS
Faculty of Science and Technology

Diagnosis of Bifacial PV Modules Using Photoluminescence Imaging from the Rear in Direct and Diffuse Irradiance

Mirabai Hillestad
Environmental Physics and Renewable Energy

PREFACE

This master's thesis marks the culmination of my education in Environmental Physics and Renewable Energy at The Norwegian University of Life Science (NMBU).

I would like to express my gratitude to all those who have contributed with inspiration, motivation, and deeper understanding, as well as to those who have supported me during this period.

I would like to extend a special thanks to my supervisor Ingunn Burud and my co-supervisor Espen Olsen for introducing me to an exciting field of study and for guiding me through my last semester here at NMBU.

I would also like to thank Marija Vuković for being a great inspiration to my master thesis, for sharing her knowledge in this field, and for generously devoting her time to give me valuable input.

My appreciation also goes to Marko Jakovljević for always taking the time to help me conduct my experiments and for his assistance in post-processing the data, and to Andreas Svarstad Fløe for his IT assistance and for allowing me to use his space and equipment.

Mirabai Hillestad

15. mai 2023

Ås

ABSTRACT

The increasing energy demand has led to a surge in solar power installations. However, solar cells are subject to damage and degradation that may not be visible to the naked eye. Consequently, various techniques have been developed to monitor solar modules to prevent unknown damages from reducing the efficiency of a solar power plant. Photoluminescence has several advantages over other techniques, providing detailed and spatial information on various types of damage in a solar cell module. The technique has been exploited with several approaches, but the built-in IV-curve sweep in the inverter is proven to be a non-invasive diagnostic method that does not disturb the power production.

This thesis explores methods that potentially make photoluminescence diagnostics more efficient, flexible, and/or accurate. The thesis includes experiments on imaging four bifacial PERC modules from the rear side under direct and diffuse light conditions at Søråsjordet in Ås. The thesis also investigates whether the PCC algorithm can increase the accuracy of the images and whether the effect is enhanced with a filtered reference signal.

The results indicate that it is possible to obtain a respectable signal-to-noise ratio from the backside of the modules under both direct and diffuse irradiance, albeit with lower photoluminescence signals than from the front. However, it has been observed that high signals are not necessary to perform an analysis of a processed image of a module.

Several practical challenges were encountered during backside image acquisition that requires further development for the method to be beneficial. The methods are not replaceable for front-side module imaging or direct irradiance image acquisition. However, the analyzable images provide additional information that can be useful for comprehensive diagnostics.

The PCC algorithm was found to produce less noisy images with better separated module and background pixels. This effect was enhanced when the reference signal was smoothed using the Savitzky-Golay filter.

SAMMENDRAG

Økt etterspørsel etter energi har ført til økt utbygging av solkraft. Solcellepaneler er utsatt for skader og degradering som ikke alltid er synlige for det blotte øye. Som et resultat er det utviklet flere teknikker for å overvåke solcellepaneler, slik at ukjente skader ikke forverrer virkningsgraden i et solcelleanlegg.

Photoluminescence har flere fordeler som andre teknikker ikke har. Teknikken er brukt med forskjellige tilnærminger, men å bruke den innebygde IV-kurvesveipen i vekselsretteren har vist seg å være en metode som ikke forstyrrer produksjonen. Dette er svært fordelaktig i diagnostiseringen av et produserende anlegg. Samtidig gir teknikken detaljert og romlig informasjon om forskjellge typer skade i en solcellemodul.

Denne masteroppgaven utforsker metoder som potensielt kan gjøre diagnostiserngen via photoluminescence mer effektiv, fleksibel og/eller nøyaktig. Det er i den anledning eksperimentert med avbildning i direkte og diffust sollys fra baksiden av fire tosidige PERC-moduler på Søråsjordet i Ås. Det er også udersøkt om PCC-algoritmen kan øke nøyaktigeten i bildene, og om effekten blir enda sterkere med filtrert referansesignal.

Resultatene viste at det er mulig å få et respektabelt signal-til-støyforhold fra baksiden i både direkte og diffus irradians, men med lavere photoluminescence-signaler enn forfra. Det er dog observert at det ikke er nødvendig med høye signaler for å utrette en analyse av et prosessert bilde av en modul.

Det fremkom flere praktiske utfordringer ved bildetakning fra baksiden av modulene som krever videre utvikling for at metoden skal være gunstig. Det er sett at metodene ikke er erstattelige for bildetakning fra fremsiden av modulen eller bildetakning i direkte irradians, men at de analyserbare bildene gir en annen informasjon som kan være nyttig for en mer utfyllende diagnostisering.

PCC-algoritmen viste seg å gi mindre støyede bilder med bedre adskilte modul- og bakgrunnspiksler. Denne effekten ble forsterket da referansesignalet ble utjevnet med Savitzky-Golay-filteret.

CONTENTS

LIST OF FIGURES

LIST OF TABLES

ABBREVIATIONS

List of all abbreviations in alphabetic order:

- **Al-BSF** Aluminum Back Surface Field
- **c-Si** Crystalline Silicon
- **DM** Degradation Mode
- **dPL** Difference Photoluminescence
- **EL** Electroluminescence
- **IR** Infrared
- I_{SC} Short Circuit Current
- **LED** Light Emitting Diode
- **LID** Light Induced Degradation
- **MOSFET** Metal–Oxide–Semiconductor Field-Effect Transistor
- **MPP** Maximum Power Point
- **MPPT** Maximum Power Point Tracker
- **OC** Open Circuit
- **PCC** Pearson Correlation Coefficient
- **PERC** Passivated Emitter and Rear Cell
- **PID** Potential Induced Degradation
- **PL** Photoluminescence
- **PV** Photovoltaic

- **SC** Short Circuit
- **SG** Savitzky-Golay
- **SNR** Signal-to-Noise Ratio
- **UAV** Unmanned Aerial Vehicle
- **UVF** Ultraviolet Flouresence
- V_{OC} Open Circuit Voltage
- V_{MPP} Maximum Power Point Voltage

CHAPTER

ONE

INTRODUCTION

The need for more energy in the world is undeniable and it is increasing rapidly [1]. It is necessary to find sustainable and renewable energy sources to meet this demand. Solar power has emerged as a promising and major contributor to the development of power infrastructure with its ability to provide an abundant and clean source of energy [2]. The development of solar power infrastructure has become a critical concern for governments and businesses globally, with the potential for solar power to become a significant contributor to the world's energy supply [3]. According to IEA's net zero pathway, 20% of the world's future energy supply will come from solar energy in 2050, requiring a 20-fold increase [4], which makes it essential to understand and optimize the technology that supports this development.

However, the degradation of solar cells is an issue and a significant concern. During its lifetime, a photovoltaic (PV) module is exposed to various external stresses in which some being common causes of cell deterioration which leads to a decrease in the efficiency of the solar cells. The external stresses may come from sources such as temperature changes (from day to night and from summer to winter), mechanical stress, stress from agents transported via the atmosphere, moisture and humidity [5] as well as hot spots caused by partial shading of the PV module [6]. To avoid that the PV modules are exposed to these factors over time, it is important to monitor them to ensure that the production of power is not compromised by unknown defects in the modules, and to ensure that optimal production efficiency is maintained. Finding methods to monitor the performance and diagnose solar cells in an accurate and efficient way is crucial. It is important to develop methods where increasing accuracy and efficiency do not come at the expense of each other.

Several PV monitoring methods have been developed over the past years; visual inspection, current-voltage measurements, UV fluorescent (UVF), thermography (IR), and electroluminescence (EL) imaging are relatively mature techniques [7]. However, these methods involve some disadvantages that can be avoided by using photoluminescence (PL). When visually inspecting solar PV, only glass breakage, and other optical degradations are detectable. When measuring the current-voltage, only the performance data is obtained. Only materials that can absorb UV can create a UVF effect [7], and UVF only detects cracks if the PV module has had a longtime exposure to UV [8]. Thermography using infrared cameras is an efficient way to gain a large-scale overview, using unmanned aerial vehicles (UAV) for instance, however, the method only detects hot-spots in the solar PV [8].

In order to achieve high-resolution and spatially resolved information about the solar module, including potential induced degradation (PID), light induced degradation (LID), cracks, series resistance effects and bypass diode failure, luminescence-based methods are fulfilling techniques [8, 9]. EL imaging will result in detailed information such as with PL, but the method requires that the module is either disassembled and analyzed in a lab setting, or that the module/string of modules is disconnected from the power production and connected to a power supply on site, but with no sun or ambient light [10, 11]. This means that on-site EL inspections often are carried through at night time when the power production is low/off and therefore cannot serve as a power supply to the EL inspection. Because it is less invasive, PL inspection has the potential to be a faster and more flexible method than EL [12].

Using PL to diagnose PV modules has been executed in different ways using different image acquisition and illumination techniques. It has been used laser [13, 14], light emitting diode (LED) [14, 15, 16, 17] and metal–oxide–semiconductor field-effect transistor (MOSFET) [18]. Using a LED device included switching the current in a contactless way by shading a control cell. This allows only one substring by one substring to be tested, and the imaging may not happen fast enough for the irradiance to be constant. By using a MOSFET, one could obtain images in a shorter time frame to avoid changes in irradiance during the image acquisition, but the method requires an electrical connection that interrupts power production. However, the I-V curve sweep of the string inverter has recently been exploited [19], allowing for more than only two operating points to be acquired. This method can make the PL image acquisition non-invasive and competitive in PV module diagnosis techniques.

To further improve the efficiency and flexibility of PV module diagnosis, it is desirable to investigate the possibilities of conducting the image acquisition in different circumstances, and from different perspectives. Outdoor PL imaging has shown that bifacial PERC modules emit PL signals from the rear [19], which is a remarkable finding in the context of flexible diagnosis of PV modules. This opportunity may have advantages that will improve the image acquisition, such as eliminating risks of shadowing the modules from the front while the image acquisition is in progress.

EL imaging has shown that different severity of cell damages appear with different applied currents (I_{SC} and $I_{0.1SC}$) [20] and that the different currents correspond to direct and diffuse irradiation (1000 W/m^2 and 100 W/m^2), respectively [21]. The opportunity to gain results from images taken in diffuse irradiance is investigated because a) it will potentially show different damage severity results than images taken in direct irradiance and b) it will potentially increase the flexibility of the diagnosis method. Especially in Norway, this would be an opportunity to reduce the limitation that comes with narrowing down the image acquisition time to days with steadily direct irradiance only. It is also assumed that imaging bifacial PV modules from the rear will benefit from diffuse irradiance because of unwanted effects on the images when the lens is pointed directly toward the sun.

Using differential PL (dPL) images and the subtraction method as a way of detecting degradation in solar cells requires manually processing the data. A way to further streamline image processing is the Pearson correlation coefficient (PCC) algorithm. The method can contribute to easier implementation of the processing in real-time because it has the potential to be unsupervised [12].

1.1 Objective and Project Description

The objective of this master's thesis is to investigate and gain a comprehensive understanding of the potential and constraints associated with using PL imaging to monitor degradation mechanisms in photovoltaic modules. Specifically, the thesis aims to explore methods that can potentially improve the diagnosis of PV modules by making the implementation more flexible, more accurate and/or more efficient. The thesis will focus on acquiring images of both the front and rear of bifacial modules under different lighting conditions, including diffuse and direct irradiance. These images will be used in the dPL and the PCC algorithms. The Savitzky-Golay filtering technique will be tested in an attempt to improve image quality and accuracy. The quality of the results will then be quantified to enable a comparison of the images, with the aim of answering the research questions.

1.2 Research Questions

The research questions to be answered in this thesis are

- How strong is the PL signal obtained from the rear, and is it possible to gain as good or better quality of the PL images taken from the rear as from the front?
- If yes, will it result in higher quality if the image acquisition is conducted in diffuse or direct irradiance?
- Will PL images acquired from diffuse and direct irradiance correspond to EL images acquired with $I_{0.1SC}$ and I_{SC}, respectively, and hence provide different information about the solar cells?
- Will the PL images be of better quality if they are processed with PCC or dPL?
- Are the PCC images of better quality if the reference signal is smoothed via the Savitzky Golay filtering?

CHAPTER

TWO

THEORY

This chapter elaborates on the theoretical principles behind PV technology, as well as the underlying mechanisms of photoluminescence. The theory behind the methods that are used to analyze and improve PL images is presented.

2.1 Working Principle of Solar Cells

Semiconductors

A solar cell consists of semiconductors, which are a type of material that has an electrical conductivity between that of a conductor and an insulator. Silicon is one of the most commonly used semiconductors in the electronics industry due to its abundance and predictable behavior. Silicon is the second most abundant element in the Earth's crust, making up almost 30% of its mass [22]. Its occurrence on Earth is primarily in the form of silicon dioxide, which is found in rocks, sand, and quartz.

The band gap energy of silicon is 1.12 electron volts (eV) at room temperature (300K), which is the energy required to move an electron from the valence band to the conduction band [23]. This property makes it a suitable material for producing electronic devices such as transistors, solar cells, and microprocessors.

The pn - junction

A pn-junction is a type of semiconductor junction formed by doping a region of a semiconductor material with impurities such as boron or phosphorous to create two regions of opposite electrical conductivity. Boron is used as an acceptor impurity in the doping process, which creates p-type material. On the other hand, phosphorous is used as a donor impurity to create n-type material. When the two

regions are brought into contact, a depletion region is formed at the interface due to the diffusion of electrons and holes across the junction. The depletion region is depleted of mobile charge carriers, which creates an electric field that prevents further diffusion of carriers. When the pn-junction is exposed to light, photons are absorbed, and electron-hole pairs are generated in the bulk region. The separated electron-hole pairs are then collected by the electric field and produce a current, which is the basis for solar cells. By controlling the doping concentrations and thickness of the depletion region, the efficiency of the solar cell can be optimized.

Recombination mechanisms

Recombination in a silicon solar cell occurs when separated electrons and holes recombine, which reduces the efficiency of the cell. One of the most significant recombination mechanisms is band-to-band recombination, which is an unavoidable process that occurs when electrons in the conduction band recombine with holes in the valence band. This mechanism is illustrated in Figure 2.1.1. This process can occur through different channels such as radiative and non-radiative recombination. Radiative recombination involves the emission of a photon with an energy similar to the band gap energy, while non-radiative recombination involves phonon release which increases heat loss. For instance will silicone with a band gap energy of 1.12 eV emit photons with a wavelength that complies with this energy. While some non-radiative recombination can be reduced through careful cell design and processing, band-to-band recombination is an inherent property of the material and cannot be eliminated.

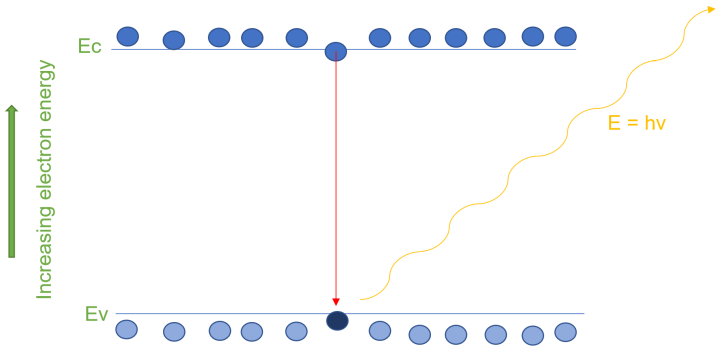

Figure 2.1.1: Band-to-band recombination mechanism.

Luminescence

Luminescence is a result of radiative recombination and is the process by which a substance emits light as a result of energy absorption. It is a broad term that encompasses different mechanisms such as fluorescence, phosphorescence, and bioluminescence. Luminescence has many applications, including in imaging, sensing, and lighting technology. In photoluminescence, the band-to-band recombination is exploited and the photoluminescence is a result of electron-hole-pair recombination which leads to emitting photons.

Knowing that light consists of energy quanta, or photons, one can calculate the wavelength of the photons emitted from recombination in silicone, using the following equation [24]:

$$E = h\nu = \frac{hc}{\lambda} \tag{2.1}$$

where E is the quantum energy, h is Planck's constant, λ is the wavelength of the photon and ν is the frequency of the electromagnetic radiation. Using Equation 2.1 to convert the band gap energy of 1.12 eV, a wavelength of approximately 1150 nm is obtained.

Imaging with a camera that can capture radiation with a wavelength of 1150 nm, one can perceive the radiative recombination effects happening in a solar cell.

2.2 Solar Spectre and Water Absorption

The wavelength range of 1100-1150 nm has a low occurrence in the global solar irradiance, as shown in Figure 2.2.1a [25]. This is due to the absorption of electromagnetic radiation in water, which coincides with the wavelength of PL signals. However, more than 95% of the radiation that the camera captures in this wavelength range is due to sunlight reflected on the silicon solar module, and 5% is the actual PL signal emitted from the solar cells, as illustrated in figure 2.2.1b. This implies that most of the electromagnetic radiation between 1100-1150 nm captured by the camera is noise and not the PL signal we are looking for. Therefore, it is desired to extract noise and reflections from the sun.

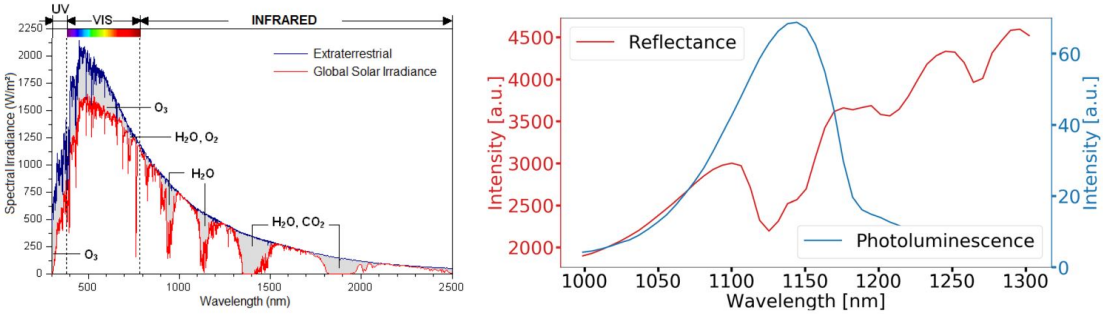

(a) Standard solar spectre [25].

(b) Spectral distribution of PL signal and reflectance of a silicon solar module [19].

Figure 2.2.1: The standard solar spectre provided by The American Society for Testing and Materials [25] is shown in (a), where the red line is the global solar irradiance. A spectral distribution of the PL signal (blue) and the reflectance (red) of a silicon solar module is shown in (b).

2.3 Photoluminescence Signal

In order to extract the actual PL signal from noise and reflections from the sun (or other illumination sources), one must consider the extracted current density. However, signals with other wavelengths than the emitted PL signal can be excluded through optical filters.

The extracted current density, J, of a solar cell is given by

$$J = J_{SC} - J_0 exp^{\frac{V_{d,A}}{V_t}} \tag{2.2}$$

where J_{SC} is the short circuit current density, J_0 is the dark current density, $V_{d,A}$ is the diode/junction voltage of region A and V_t is the thermal voltage [19, 26].

The average PL signal of a solar cell area A is given by

$$PL_A = C \cdot exp(\frac{V_{d,A}}{V_t}) + PL_{offset,A} \tag{2.3}$$

where C is a calibration constant depending on i.e. the carrier lifetime and geometry and PL_{offset} is the PL signal caused by diffusion-limited carriers [19, 26].

Rearranging equation (2.3) and solving for $V_{d,A}$, in order to replace $V_{d,A}$ in equation (2.2) results in

$$J = J_{SC} - \frac{J_0}{C}(PL_A - PL_{offset,A}). \tag{2.4}$$

Equation 2.4 describes the level of current extraction in the solar cell and can

be adjusted to different operating points of the solar cell. Naming two different operating points 1 and 2, equation 2.4 can be written as

$$J_1 = J_{SC,1} - \frac{J_{0,1}}{C_1}(PL_{A,1} - PL_{offset,A1}). \tag{2.5}$$

and

$$J_2 = J_{SC,2} - \frac{J_{0,2}}{C_2}(PL_{A2} - PL_{offset,A2}). \tag{2.6}$$

respectively. The calibration constant C remains unchanged through the different operating points, and can be determined from an image in open circuit condition and from the open circuit voltage, which means that $C_1 = C_2 = C$ [19]. The same occurs for the illumination condition. It remains unchanged through the operating points and J_{SC} is therefore considered constant; $J_{SC,1} = J_{SC,2} = J_{SC}$.

The dark current density is also considered constant; $J_{0,1} = J_{0,2} = J_0$ [19]. The PL signal caused by diffusion-limited carriers, $PL_{offset,A}$, is considered constant through the two operating points so that $PL_{offset,A1} = PL_{offset,A2} = PL_{offset,A}$. $PL_{offset,A}$ can be found with an image taken during short circuit (SC) conditions.

Calculating the difference in extracted current density between the operating point by subtracting equation 2.6 from equation 2.5 we obtain the equation

$$PL_{A2} - PL_{A1} = \frac{C}{J_0}(J_1 - J_2), \tag{2.7}$$

which shows that the difference in PL signal intensity, dPL, between two operating points is inversely proportional to the extracted current density in the same two operating points. This means that the noise can be extracted and the PL signal can be captured when images in two different operating points, i.e. open circuit (OC) and SC or maximum power point (MPP), are subtracted from each other.

2.4 I-V Curves

An I-V curve is a graphical representation of the relationship between the current (I) flowing through a device and the voltage (V) applied to it. In the context of solar cells, an I-V curve shows how the solar cell responds to different levels of irradiance and temperature, providing a measure of the cell's electrical performance.

The curve typically starts at the open-circuit voltage (V_{OC}), where the current is zero and the voltage is at its maximum, and then the voltage decreases as the current increases due to the load. At short-circuit conditions, the current is at

its maximum, and the voltage is zero. A point in between these points is the maximum power point, which is illustrated in Figure 2.4.1. The shape of the curve depends on the device's electrical properties, such as its internal resistance and the presence of shunt and series resistance.

The I-V curve is a crucial tool for analyzing and optimizing the performance of solar cells, as it provides information on the cell's maximum power point, where the product of the current and voltage is at its highest, and the fill factor, which is a measure of the cell's efficiency.

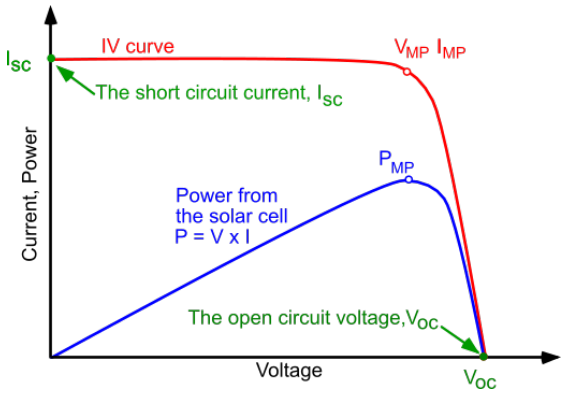

Figure 2.4.1: Characteristic I-V curve of a solar cell.

Maximum Power Point Tracking

The maximum power point tracker is not a physical component but a built-in functionality in string inverters. The operating point is defined as the voltage and current values in which the PV module operates. Looking at Figure 2.4.1, this point on the I-V curve correlates to a point on the power-voltage curve, as $P = I \cdot V$. In order to obtain the MPP, one should find the current and voltage values correlating to the apex of the power-voltage curve.

For the module to operate in MPP, the voltage needs to be forced to operate at the MPP (V_{MPP}). It is important to remember that the MPP is dependent on ambient conditions such as temperature and irradiance, and the MPP will therefore fluctuate as the circumstances change. Therefore, the MPP trackers exist so that the module is adjusted to the MPP.

There are several ways and algorithms to find V_{MPP}, but experimental studies [19, 12] have found that some type of inverters will sweep through the complete I-V curve in order to find the MPP. This will give insight into several operating points, which are needed when imaging photoluminescence.

2.5 Bifacial Solar Cells

The monofacial silicon solar cell with an aluminum back surface field (Al-BSF) was dominant on the market for a long time[27]. This is a crystalline silicon cell made of p-type silicon and a back surface that is opaque to light [27], as seen on the left side of Figure 2.5.1. This means that only light entering from the front will affect the cell.

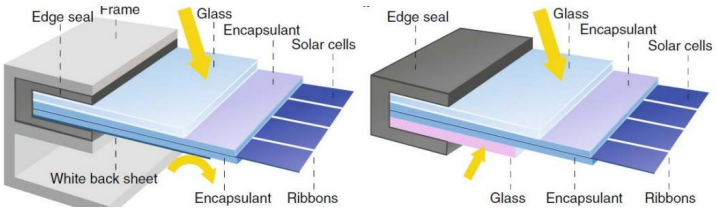

Figure 2.5.1: Bifacial solar cells are partially metalized on the rear side, and do not have an aluminum back surface that prevents the light to enter from the rear side [27].

Bifacial solar cells are a more advanced type of cell design, illustrated on the right-hand side of Figure 2.5.1. This type of solar cell only requires partial metallization on the rear side of the cell, allowing more light to enter from the rear as well as light entering the front, as illustrated in Figure 2.5.2. This is beneficial especially in areas with high albedo, as the scattered light from the ground will increase the light entering the rear side of the cell.

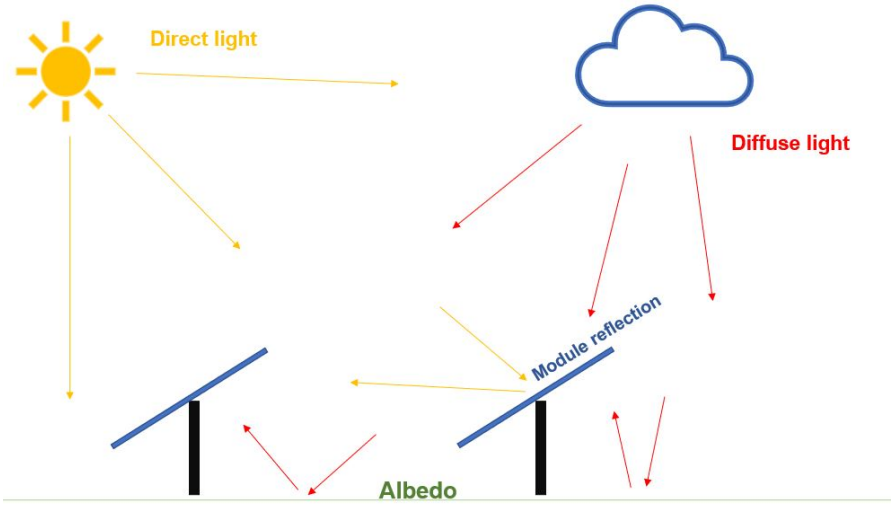

Figure 2.5.2: Bifacial solar cells absorb direct sunlight on the front side as well as scattered light from the ground and reflected light from other PV modules on the rear side.

The Passivated Emitter and Rear Cell can be made bifacial and therefore able to absorb light from both the rear and the front side of the solar module. This typically increases the efficiency by 25-30 % [27].

2.6 Pearson Correlation Algorithm

Using correlation analysis is shown to be robust and useful when trying to reduce and exclude noise [12, 28], and also has the potential to be an unsupervised method of processing PL images. This means that an image series can be processed through the algorithm without any pre-processing [12]. The main goal of the PCC algorithm is to separate PL signals coming from the PV module from other signals in the background. This is possible by calculating the correlation between two variables; the intensity values from one pixel in a series of images, X_i, and the reference values, Y. The following equation is used in order to calculate the correlation [12]:

$$\rho = \frac{\sum_{i=1}^{N}(X_i - \bar{X})(Y_i - \bar{Y})}{\sqrt{\sum_{i=1}^{N}(X_i - \bar{X})^2}\sqrt{\sum_{i=1}^{N}(Y_i - \bar{Y})^2}} \tag{2.8}$$

where, in this context, Y is the mean image count which is used as the reference, X_i is the intensity value of one specific pixel in a series of images, ρ is the correlation coefficient and N is the number of images in the image series.

The method is applicable when the PL signal undergoes a distinct change in intensity compared to the background, which is the case during the I-V curve sweep process. The correlation coefficient, ρ, is quantifying the extent of linear similarity between the variables and is a number between -1 $\leq \rho \leq$ 1 [28]. This means that the pixels in the PV module should correlate more with the reference than the pixels in the background correlates with the reference, as seen in Figure 2.6.2. The variables in the series of images are illustrated in Figure 2.6.1, which shows that the background pixels will have a lower ρ value than the module pixel.

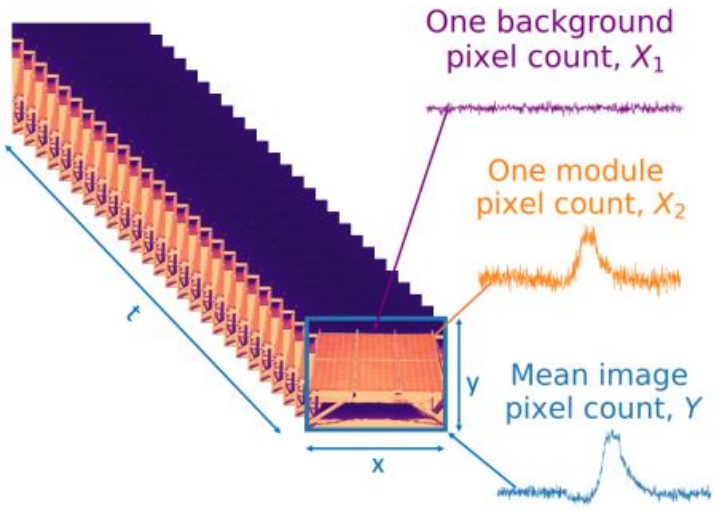

Figure 2.6.1: Pearson Correlation Coefficient. The images have x*y pixels and the number of images is t [12].

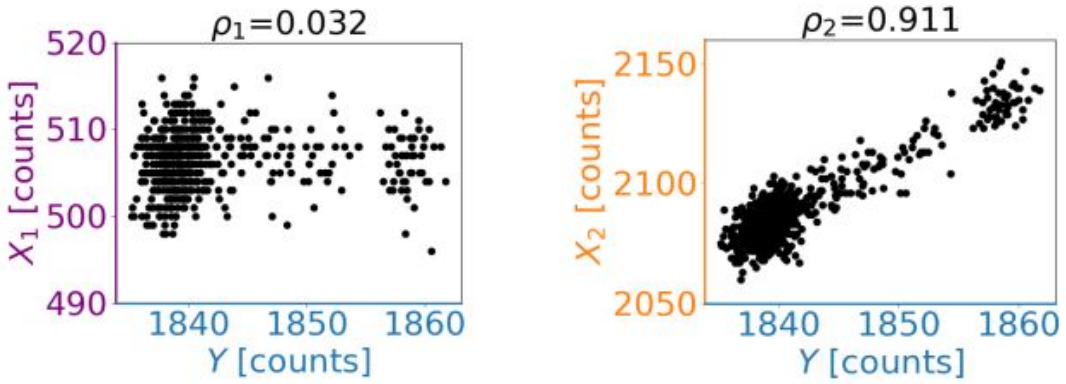

(a) The correlation between the background pixels and the reference values [12].

(b) The correlation between the module pixels and the reference values [12].

Figure 2.6.2: The correlation coefficient ρ is higher between the module pixel and reference than between background pixel and reference.

This theory is more clear when the module is dominant in the image, i.e. the module contains more pixels than the background. According to an experiment on what extent the module needs to be dominant in order to reduce background noise, one can obtain a high PCC value with as little as 20% of the module covering the image [12].

Savitzky Golay Smoothing

Savitzky-Golay filtering is a smoothing technique used for retrieval of a signal structure while also excluding noise [29]. The mean image intensity may have some noise, even with 640x512 pixels. It is therefore recommended that the reference signal is smoothed out in order to retain the shape of the PL signal, but remove the outliers [12]. In order to determine the trend signal, one must choose a window size and a polynomial order [30]. The window size represents the number of values taken into account when replacing the original value with the new one, which is fitted with the chosen degree of polynomial.

2.7 Signal-to-Noise Ratio

Signal-to-noise ratio (SNR) can be used as a measure of quality in an image by analysing the power of the signal in a noisy environment [31, 32, 33]. This is important in order to validate the obtained signals and to distinguish the signal from the noise that might distort the signal.

The SNR evaluation in this thesis is based on the equation [33]:

$$SNR_{avg} = \frac{\sum_k (avg_{i \in N}(OC_i(k) - SC_i(k)))}{\sum_k (|avg_{i \in N_1}(OC_i(k)) - avg_{j \in N_2}(OC_j(k))| \cdot \sqrt{0.5} \cdot (\frac{2}{\pi})^{-0.5})} \tag{2.9}$$

where N represents the number of images in an OC or SC image stack as a whole, N_1 represents the first half of the OC images and N_2 is the second half. The equation is derived from [31] and [32] where k is the pixel count, $OC(k)$ is the intensity values in all pixels of the OC image and $SC(k)$ is the intensity values in all pixels of the SC image, which is used as the background parameter.

According to SNR criteria from [31] there are some guidelines for minimal SNR values dependent on the measurement application and circumstances. For outdoor measurements the SNR_{50} should be greater or equal to 5. In this thesis, it is assumed that the same number accounts for SNR_{avg} and for outdoor PL imaging.

[33]

CHAPTER

THREE

METHODS

This chapter will firstly list and explain the equipment used to conduct the experiments, secondly explain the methods that are used both practically and theoretically for each experiment. This includes image processing and analysis.

3.1 Instruments and Set Up

This section explains how the images were acquired, how the data was collected and which equipment was used to carry out the data collection. The experiments in this thesis were conducted on the PV modules on Søråsjordet in Ås.

PV Modules

The PV modules that were used to analyze and assess the methods were of the type JA Solar JAM72D20, which is a bifacial passivated emitter and rear cell (PERC) module [34]. The rated nominal power is 460 W, the open circuit voltage (V_{OC}) is 49.91 V (0.693 V per cell) and the short circuit current (I_{SC}) is 11.5 A. All modules, both on the north side and south side of the site, are of the same type, which is shown in Figure 3.1.1 and Figure 3.1.2. On the north side of the site, there are three modules connected to the same string inverter, hereby referred to as the PERC3 modules. Each module consists of 144 (6 x 24) cells which all appear healthy.

On the south side of the site, there is one single JA Solar JAM72D20 PERC module, hereby referred to as the PERC1 module, which is connected to the same type of inverter. The other modules (of another type) are disconnected from the string inverter during these experiments. The module is severely damaged, which is visible to the eye as cracks and broken glass surface over the solar cells, seen in Figure 3.1.2a.

(a) Rear side of the healthy modules, PERC3.

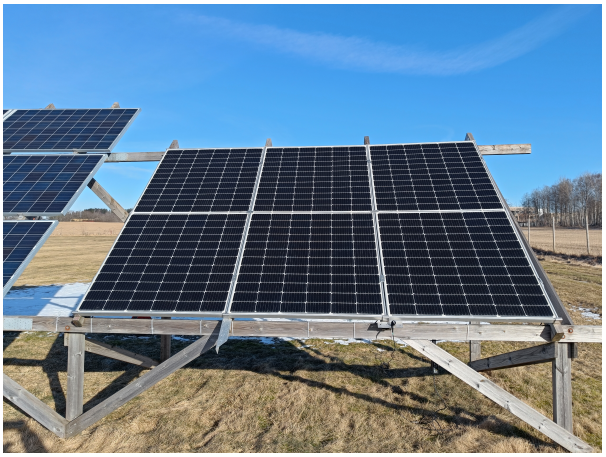

(b) Front side of the healthy modules, PERC3.

Figure 3.1.1: Figure (a) shows the rear side of PERC3, connected to the string inverter on the north side of the site, and Figure (b) shows the same modules from the front.

(a) Front side of the damaged module, PERC1.

(b) Rear side of the damaged module, PERC1.

Figure 3.1.2: Figure (a) shows the front side of PERC1 connected to the string inverter on the south side of the site and Figure (b) shows the same module from the rear.

Inverter

The string inverter that is used on the north string connected to PERC3, and on the south string connected to PERC1, is of the type Fronius Primo 3.0, which is depicted in Figure 3.1.3 (grey box on top).

Figure 3.1.3: All modules used in the experiments are connected to a string inverter of the type Fronius Primo 3.0.

The inverter has a built-in function that tracks the maximum power point, causing the inverter to carry through an I-V curve sweep in order to find the point that results in maximum power output. It then forces the voltage to stay at the spot that induced the current and voltage of maximum power (V_{MPP} and I_{MPP}). The I-V curve sweep happens approximately every 10 minutes. The I-V curve sweeps are allowing us to acquire images in several operation points, continuously, without invading the power production.

Camera

A short-wave infrared camera was used to acquire the images of the PV modules. The camera type was Raptor Photonics Owl 640S, including an InGaAs detector. It has an optical range of 900–1700 nm and a 640x512 resolution. The camera is capable of running at a high frame rate, up to 300 Hz (frames per second) in full frame resolution, enabling high speed digital video rates [35]. The camera is shown in Figure 3.1.4.

The lens was covered with a filter in order to filter out the reflected light with wavelengths that were not of interest. The filter is from Edmund Optics and has an optical density of ≥ 4.0. The filter includes an optical range of 1125-1175 nm.

Several images were first acquired during direct sunlight onto the PV modules. This resulted in the sunlight hitting directly on the camera lens, causing an unwanted effect on the images. An extra, detachable lens hood was therefore attached in order to carry out the experiment in direct sunlight again, without the sunlight making reflections on the camera lens. The lens hood is shown in Figure 3.1.4 as the red tube on the tip of the camera lens.

Figure 3.1.4: The camera that was used to conduct the experiments was the Raptor Photonics Owl 640S. The external triggering box is attached to the tripod below the camera.

Pyranometer

A pyranometer from Apogee (SP-212) was mounted on the same rig that the modules were mounted on and was moved to the same side of the site (north and south) where the image acquisition took place. The pyranometer was screwed as close to the modules as possible, in order to have as accurate irradiation data as possible. The mount of the pyranometer is shown in Figure 3.1.5. The pyranometer was used in order to compare variation in current flow through the PV modules and variation in irradiance. This is helpful when assessing signals and noise, and distinguishing between the current increasing or decreasing due to the I-V curve sweep induced by the inverter and due to irradiation fluctuations. All measured irradiances are summarised in Table A.1 in Appendix A.

Figure 3.1.5: The Apogee pyranometer that was used is screwed right below the modules in order to capture the same irradiance as the modules.

Set Up

The camera is placed at a distance as close to the modules as possible so that the resolution is still high, but so that the objects (the modules) are fully captured. At the same time, the angle is such that the direct sunlight does not hit the camera lens. This had to be taken into account, even with the lens hood on. In diffuse light, the camera was directed directly toward the PV modules.

The camera was connected to a frame grabber, an external trigger and to power via the computer. The frame grabber made the computer able to grab the high frequency frame rate of the camera, which can be as high as 300 frames per second. The external trigger is a device used to trig the camera to capture images at a desired rate. The external trigger is also connected to power. The external trigger device is shown in Figure 3.1.4 as a blue plate with an orange box on it, attached to the camera tripod.

A clamp meter was connected to the module's power cable and to an ampere meter that would send the current data to be read off of the computer. A simplified illustration of the setup is shown in Figure 3.1.6.

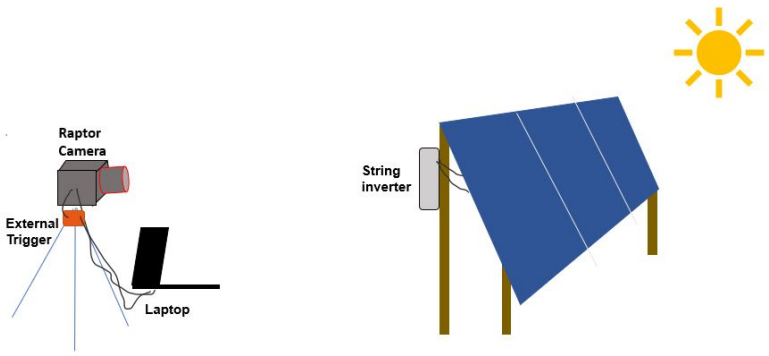

Figure 3.1.6: An illustration of the instruments and how it is set up.

Software

EPIX XCAP and EPIX PIXCI were used to adjust the frame rate, number of images acquired and integration time (exposure time) as well as to display the object/live capture of the Raptor camera on site. Labview was used to display the current and irradiance data, which was converted to a tdms-file in order to read the data into Python. This made it possible to collect the images that corresponded to the I-V curve sweeps. Python was used to process, display and analyze the images.

3.2 Procedure

Images of the PV modules were collected on three different days. The first data set was collected on a day with no direct sunlight, only diffuse irradiance. The second and third data sets were collected with cloudless conditions and direct sunlight. The second data set was discarded because of some unforeseen and unwanted effects concerning the direct sunlight on the camera lens. This was fixed by 3D-printing a customized lens hood for the third data collection.

When all equipment was set up and connected, the camera and software had to be adjusted and prepared for the image acquisition. This included adjusting the focus of the lens, adjusting the lens hood, and adjusting the exposure time (integration time in XCAP). The exposure time adjustment has to account for the sun's movement, which could affect the saturation of the image.

Then the number of images and the rate at which the images were to be captured was chosen. The choice of values should account for the time it takes between every I-V curve sweep that the string inverter performs, and the desired amount of images for the different operation points in the I-V curve sweep. The Fronius Primo 3.0 inverter performs an I-V curve sweep to track the maximum power point every 10 minutes, and the sweep has a duration of approximately

2 seconds. To make sure that at least two I-V curve sweeps were captured, the image acquisition needed a durability of at least 20 minutes. In order to capture 100-200 images of the I-V curve sweep, the frame rate was set to a minimum of 150 Hz. The number of images captured was 200,000 so the duration was 1,333 seconds or 22.2 minutes, which covered two to three I-V curve sweep samples.

Because of the extensive amount of images and the high frame rate, the images were saved as a video file on site, which was later unpacked into separate images. When this procedure was conducted on both the PERC3 modules and the PERC1 module, in direct and diffuse irradiance, all images were unpacked and LabView was used to visualize which images corresponded to the drop of current (i.e. the I-V curve sweep). 1,000-2,000 images around the current drop were collected for each case. The image folders, the current files and the irradiance files were then read into Python and were ready to be processed and analyzed.

Images from the front of the PV modules were received from previous projects and are collected in the same way, so that the processing and analysis are conducted in the same way.

3.3 Image Processing

Figure 3.3.1 demonstrates how the images look like when they are unpacked and before they are processed.

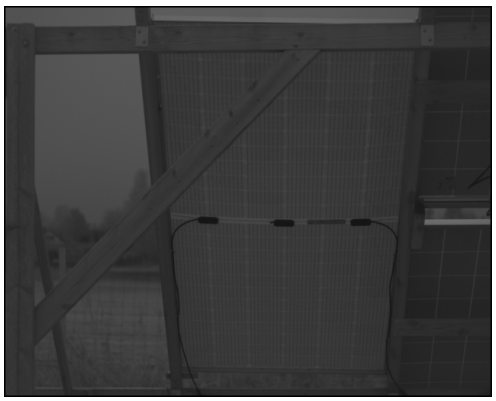

(a) Raw image of the damaged module.

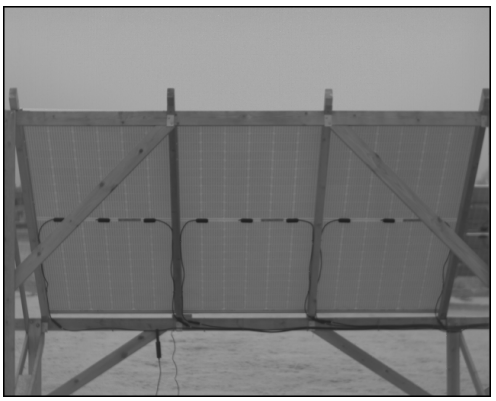

(b) Raw image of the healthy modules.

Figure 3.3.1: Raw and unprocessed images of all four modules taken in diffuse irradiation conditions.

The folder with the images from around the I-V curve sweep is read into Python and the mean image intensity values through the entire image series are plotted in a graph in order to visualize where the PL signal is high and low, i.e. where the extracted current is low and high. The selection of images was based on the

PL intensity graph.

After the image processing, all images are to a certain extent adjusted in the brightness scale in order for the PL signals to be observable, but without reaching saturation in any pixels. In order to compare some of the images, they are perspective transformed and flipped, so that the solar cells in the images from front and back correlate.

dPL images

In order to obtain the dPL images, a shorter snippet of the operation points (high and low PL signal, respectively) is chosen for each case. The values are averaged in a new image. These two images are subtracted from each other to obtain the dPL image. The operation points are called OC and SC.

PCC images

In order to obtain the PCC images, a snippet of the whole I-V curve sweep, and a few images before and after, are chosen as the image range to undergo the PCC algorithm. The image range is called N.

PCC Images with Savitzky-Golay Smoothing

In order to investigate whether the smoothing filter has a positive effect on the PCC image from the rear of the modules, the mean pixel intensity value, i.e. the reference signal, is smoothed using the SG smoothing filter. The new reference signal is then used in the PCC algorithm, resulting in different PCC images.

3.4 Image Analysis

The SNR is calculated in order to analyze and compare the image qualities. The cumulative histograms are plotted in order to compare the pixel intensity distribution. Scatter plots and regression lines are plotted with the corresponding correlation coefficient in order to analyze the effect of applying the SG smoothing filter.

SNR Calculation

Prior to the SNR calculation, the background was cropped so that the calculation was in accordance with the EL imaging standard [31]. The images from the rear, especially PERC1, were further cropped in order to comply with the requirement of only containing principally active cell area, meaning that the poles and the

damaged cells were excluded. The same images that were used to obtain the dPL images (OC and SC) were used in Equation 2.9. The images from the OC condition were first split in half, and then the average was calculated for the denominator of Equation 2.9. The SNR values are summarised in Table C.1 in Appendix C.

Cumulative Histograms

The dPL and PCC images are normalized prior to the cumulative histogram calculation and plotting. The normalized cumulative histogram will visualize the pixel intensity distribution and is a tool to quantify how well the dPL and PCC images are able to distinguish between module pixels and background pixels.

Correlation coefficient and regression

The Pearson correlation coefficient is calculated, and a regression line is plotted to visualize the correlation between a) the reference (mean intensity) and a module pixel and b) the reference and a background pixel.

In order to illustrate the impact that the SG smoothing filter constitutes, a scatter plot and a corresponding regression line are made. The correlation coefficient is calculated for a comparison of the PCC image before and after the smoothing filter is applied. The correlation coefficients are summarised in Table B.1 in Appendix B.

CHAPTER

FOUR

RESULTS

In this chapter, the results are divided into four sections. Section 4.1 compares front and rear imaging. Section 4.2 presents the results from imaging in direct and diffuse irradiance, and compares them with EL images with I_{SC} and 10% of I_{SC}. Section 4.3 presents the differences between dPL images and PCC images. Lastly, Section 4.4 compares PCC images with and without smoothed reference signal.

4.1 Front vs Rear Imaging

This section will show the results of PL imaging from the rear, and compare it to the front imaging that has been conducted in an earlier study. The PL signal intensities from PERC3 and PERC1 in both direct and diffuse irradiance are compared. The dPL images are visually assessed and compared.

Direct Irradiance

Figure 4.1.1 shows a comparison of PERC3 acquired in direct sunlight. The image processing method that is used in order to obtain these images is dPL. The SNR was calculated for both images and the calculated SNR for the front image was 4.6 and the SNR for the rear image was 6.9.

Figure 4.1.1a is obtained from images acquired from the rear side of the modules. The range of images that are used is marked with red in Figure 4.1.2a, where the PL signal intensity and current flow are plotted. Figure 4.1.1b is obtained from images acquired from the front side. The range of images that are used for this image is marked with red in Figure 4.1.2b.

Both images of PERC3 are perspective transformed, meaning that the pixel coordinates are manipulated from the original images. The images are also flipped vertically so that they are directly visually comparable. However, it is noticed that the top row of cells in Figure 4.1.1a is occluded by the top pole, and several cells are partially covered by the diagonal poles.

The intensity of the front image in Figure 4.1.1b is higher than in the rear image in Figure 4.1.1a, thus the scale of the color bar is different. This is illustrated in Figure 4.1.2 where the PL signal has a higher peak in intensity for the image from the front than from the back. It is observed that the PL signal intensity peaks at approximately 1180 for the rear images and 1860 for the front images.

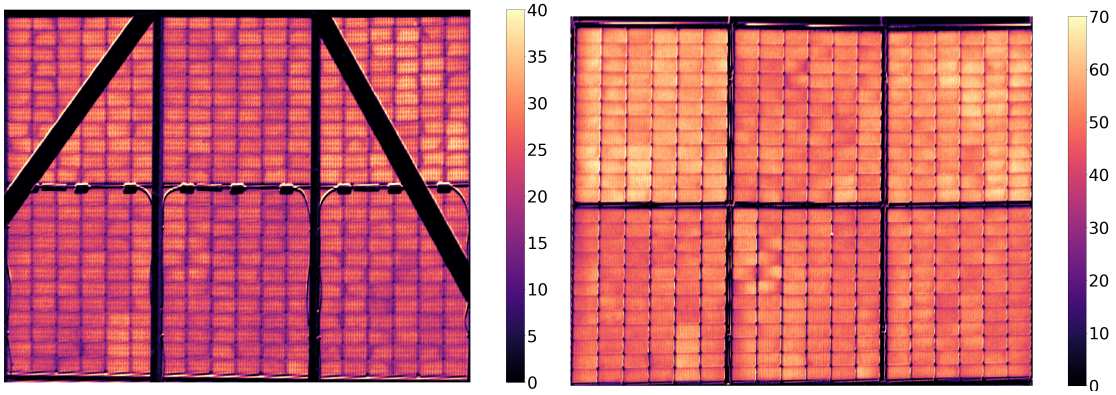

(a) Rear dPL image of PERC3 in direct sunlight.

(b) Front dPL image of PERC3 in direct sunlight.

Figure 4.1.1: Comparison of dPL image on PERC3 in direct sunlight from both sides of the modules.

The current graphs are plotted above the PL signal intensity graphs in Figure 4.1.2 for both images of PERC3. The current graph is data from the ampere meter and the PL signal graph is the intensity value of the average pixel in the entire range of images. The graphs illustrate the correspondence between low extracted current values and high PL intensity values.

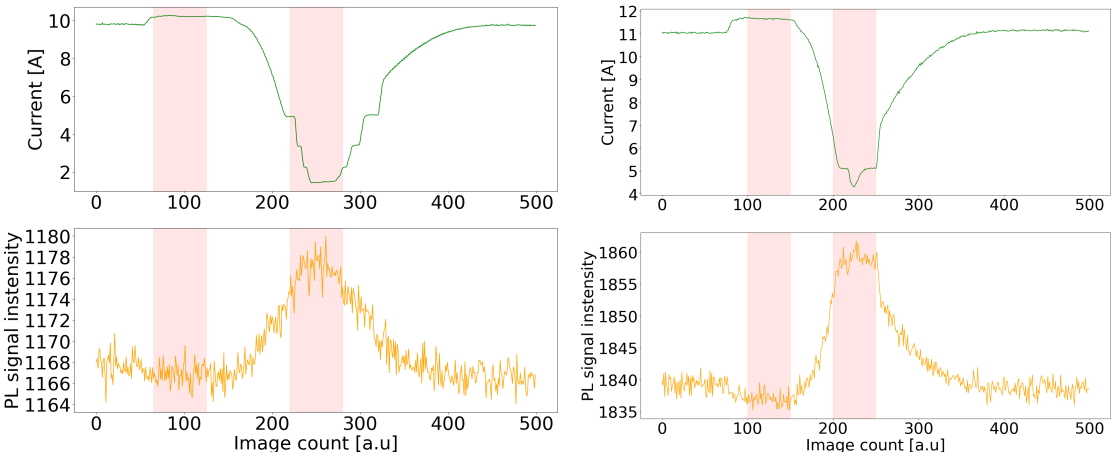

(a) Rear side of PERC3 in direct sunlight. **(b)** Front side of PERC3 in direct sunlight.

Figure 4.1.2: Comparison of the PL signal intensity and current of PERC3 in direct sunlight. Red areas represent the range of images used to produce the dPL image.

Each data point in the graphs corresponds to one image, meaning that the plots contain 500 images and 500 current data points. The images collected in order to constitute the SC image are marked with red to the left, which contained 60 images for the rear side of the module and 50 images for the front side of the module. The images collected in order to constitute the OC image are marked with red to the right. The number of images to constitute the OC image is the same amount as for the SC image; 60 images for the rear side and 50 images for the front side.

The index and amount of images for the OC image are chosen with the intention of covering the images with as high PL intensity as possible, i.e. as low extracted current as possible. The opposite accounts for the SC images, where the intention is to cover images with low PL signal intensity and high extracted current. The amount of SC images and OC images are similar in order for the SNR calculation to be in accordance with the imaging procedure criteria from [31], so there are as many background pixels as there are signal pixels.

It is noticed that the PL signal intensity graph has a higher value both in SC and OC conditions for the front side than the rear side of the modules. However, the current graph has a lower value for the front side of the modules, meaning that the modules operated with a lower current on the day that the front images were acquired. The average irradiance measured with the pyranometer mounted adjacent to the modules was 955 W/m^2 on the day of the rear imaging. This is the average irradiance during the analyzed I-V sweep. The average irradiance of the I-V curve sweep from the front was 841 W/m^2. All measured irradiances are summarised in Table A.1.

Figure 4.1.3 shows PERC1 acquired in direct irradiance from the front side and the rear side. Both images are obtained using the dPL algorithm. The range of images that are used to obtain the front image in Figure 4.1.3a is marked with red in Figure 4.1.4a. Figure 4.1.3b is obtained from images acquired from the front side and the range of images that are used for this image is marked with red in Figure 4.1.4b.

One can observe that the bus bars are more prominent in the figures of the module from the rear than in the figures of the module from the front, both on PERC1 and PERC3. Both of the images of PERC1 are perspective transformed, and Figure 4.1.3a is flipped vertically so that it corresponds to Figure 4.1.3b. However, it is noticed that the top one-and-a-half row of cells in figure 4.1.3a is occluded by the top pole, and several cells are partially covered by the diagonal pole on the right-hand side of the figure.

The scale of the color bar is different in this case as well, due to the difference of intensity of the rear image in Figure 4.1.3a, which is lower than in the front image in Figure 4.1.3b. The intensity difference is illustrated in Figure 4.1.4. It is observed that the PL signal intensity peaks at approximately 1240 for the rear images and 1890 for the front images.

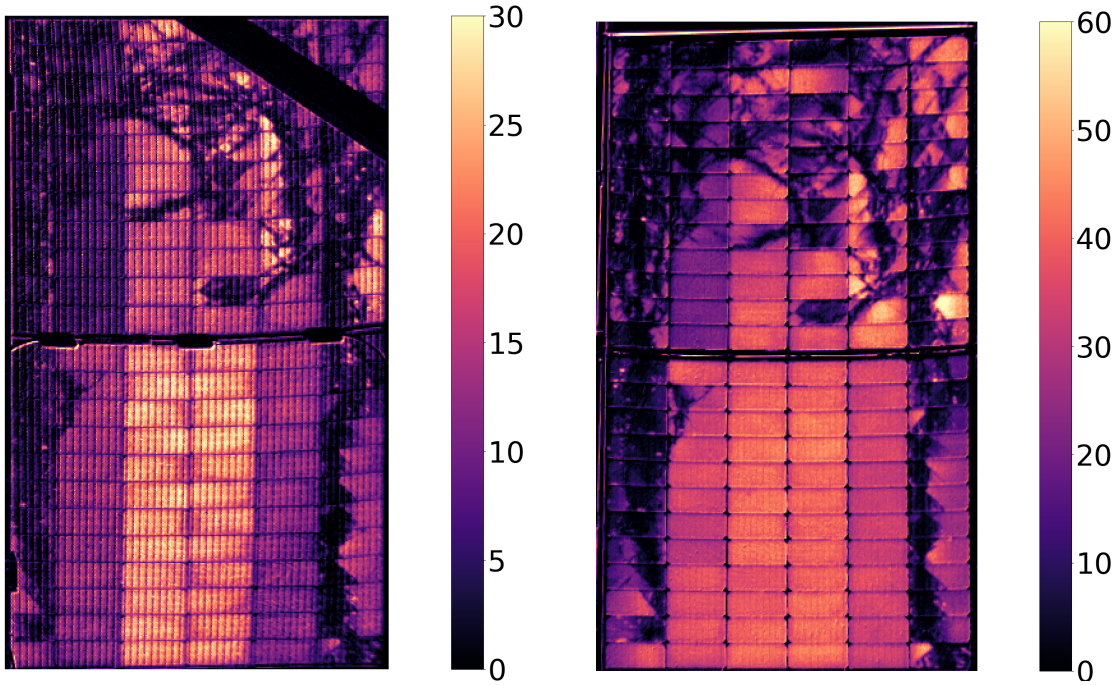

(a) Rear image of PERC1 in direct sunlight. **(b)** Front image of PERC1 in direct sunlight.

Figure 4.1.3: Comparison of dPL image on PERC1 in direct sunlight from (a) rear side and (b) front side.

The current graphs and PL intensity graphs associated with PERC1 are shown in Figure 4.1.4. The graphs illustrate great correspondence between the low extracted current and high PL signal intensity. The current level in Figure 4.1.4a and Figure 4.1.4b are in the same range and the irradiance measured on PERC1 in the case with direct irradiance and rear imaging was 1016 W/m^2. This is an average of the irradiance during the I-V curve sweep. For the front image, the irradiance was 792 W/m^2.

The images collected in order to constitute the SC image are marked in red to the left in Figure 4.1.4a and Figure 4.1.4b, which contained 25 images for the rear side of the module and 35 images for the front side of the module. The images collected in order to constitute the OC image are marked with red to the right. An equivalent amount of images are selected to constitute the OC image as for the SC image; 25 images for the rear side and 35 images for the front side.

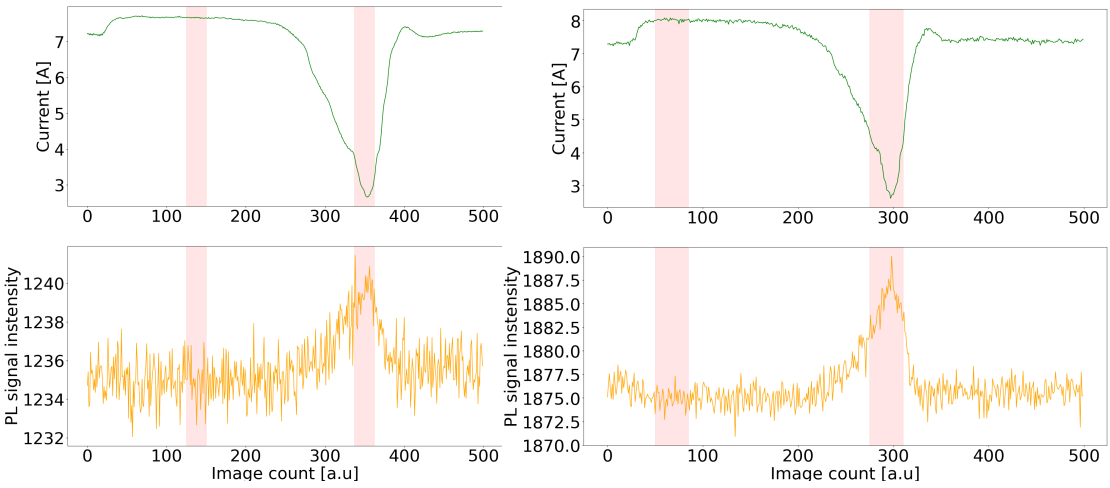

(a) Rear side of PERC1 in direct irradiance.

(b) Front side of PERC1 in direct irradiance.

Figure 4.1.4: Comparison of the PL signal intensity and current of PERC1 in direct sunlight. Red areas represent the range of images used to produce the dPL image.

Diffuse Irradiance

Figure 4.1.5 shows a comparison of PERC3 acquired in diffuse irradiance from the front and rear, both obtained with the dPL algorithm. The SNR was calculated to be 7.5 for the front image and 1.5 for the rear image.

The range of images that are used to obtain the rear image in Figure 4.1.5a is marked with red in Figure 4.1.6a, where the PL signal intensity and current flow are plotted. Figure 4.1.5b is obtained from images acquired from the front side. The range of images that are used for this image is marked with red in Figure 4.1.6b, which is the graphs of the associated current and PL signal intensity.

Both images of PERC3 in diffuse irradiance are perspective transformed. Figure 4.1.5a is flipped vertically in order to be directly visually comparable to Figure 4.1.5b. It is noticed that in this case as well, the top row of cells is covered by the top pole and several cells are partially covered by the diagonal poles.

Such as with the above cases, the intensity of the front image in Figure 4.1.5a is higher than in the rear image in Figure 4.1.5b, thus the scale of the color bar is different. This is illustrated in Figure 4.1.6 where the PL signal has a higher peak in intensity for the image from the front than from the rear. In this case, the PL signal intensity peaks at approximately 1534 for the rear images and 1985 for the front images.

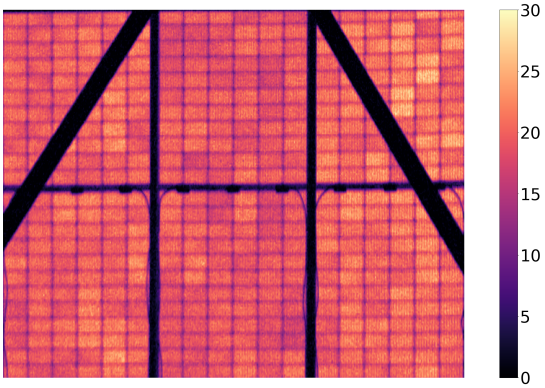

(a) Rear dPL image of PERC3 in diffuse irradiance.

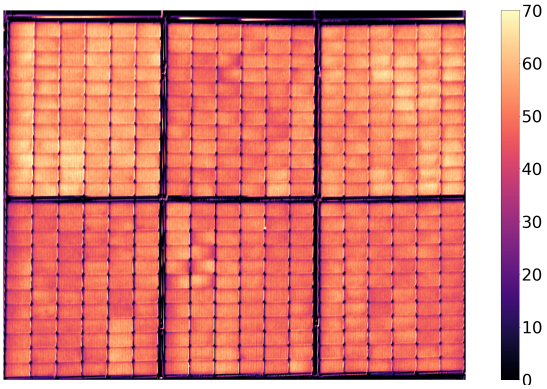

(b) Front dPL image of PERC3 in diffuse irradiance.

Figure 4.1.5: Comparison of dPL image of PERC3 in diffuse sunlight from (a) rear side of the module and (b) front side of the module.

Figure 4.1.6 shows the corresponding current graphs and the PL signal intensity graphs, both for PERC3. The images collected in order to constitute the SC image are marked in red to the left in Figure 4.1.6a and Figure 4.1.6b, which contained 40 images for the rear side of the module and 30 images for the front side of the module. The images collected in order to constitute to OC image are marked in

red to the right. The number of images to constitute the OC image is the same amount as for the SC image; 40 images for the rear side and 30 images for the front side.

The current level in Figure 4.1.6a and Figure 4.1.6b are in the same range but are slightly lower when the front images were captured. The irradiance measured on PERC3 in diffuse conditions from the rear was 72.3 W/m^2. This is an average of the irradiance during the I-V curve sweep. For the front image, the irradiance was 45.2 W/m^2, which explains the difference in current.

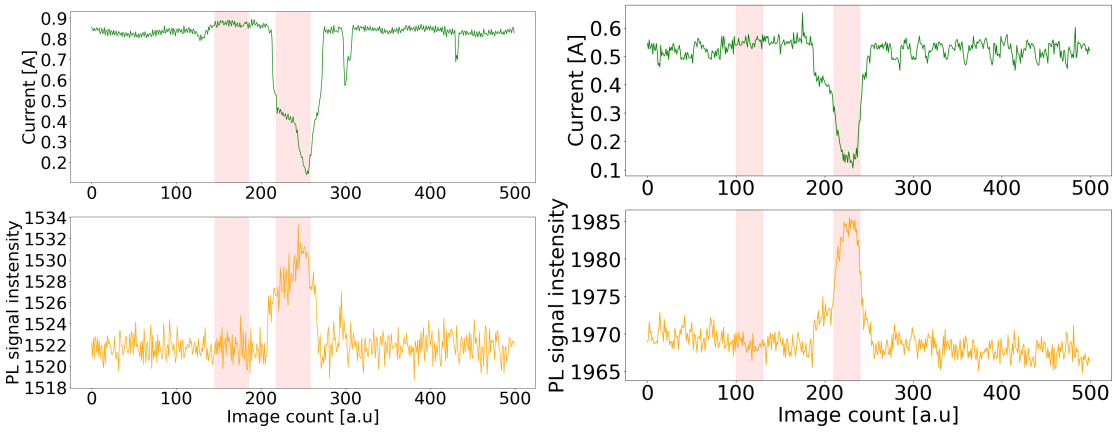

(a) Rear side of PERC3 in diffuse irradiance. **(b)** Front side of PERC3 in diffuse irradiance.

Figure 4.1.6: Comparison of the PL signal intensity and current of PERC3 in direct irradiance. Red areas represent the range of images used to produce the dPL image.

Figure 4.1.7 shows a comparison of PERC1 acquired in diffuse irradiance. The image processing method that is used in order to obtain these images is dPL. Figure 4.1.7a is obtained from images acquired from the rear side of the modules and the range of images that is used is marked with red in Figure 4.1.8a, where the PL signal intensity and current flow are plotted. Figure 4.1.7b is obtained from images acquired from the front side. The range of images that is used for this image is marked with red in Figure 4.1.8b. Both images of PERC1 is perspective transformed.

The intensity of the front image in Figure 4.1.7a is higher than in the rear image in Figure 4.1.7b, thus the scale of the color bar is different. This is explained from Figure 4.1.8 where the PL signal has a higher peak in intensity for the image from the front than from the back; the PL signal intensity peaks at approximately 1710 for the rear images and 1988 for the front images.

The current graphs shown above the intensity graphs for PERC1 in diffuse irradiance are represented in Figure 4.1.8. In both Figure 4.1.8a and Figure 4.1.8b the images chosen to create the SC image are highlighted in red on the left side. For the rear side of the module, 20 images were selected, and for the front side, 25 images were chosen. The OC image is composed of images marked in red on the right side. The number of images used to create the OC image is equal to the number used for the SC image.

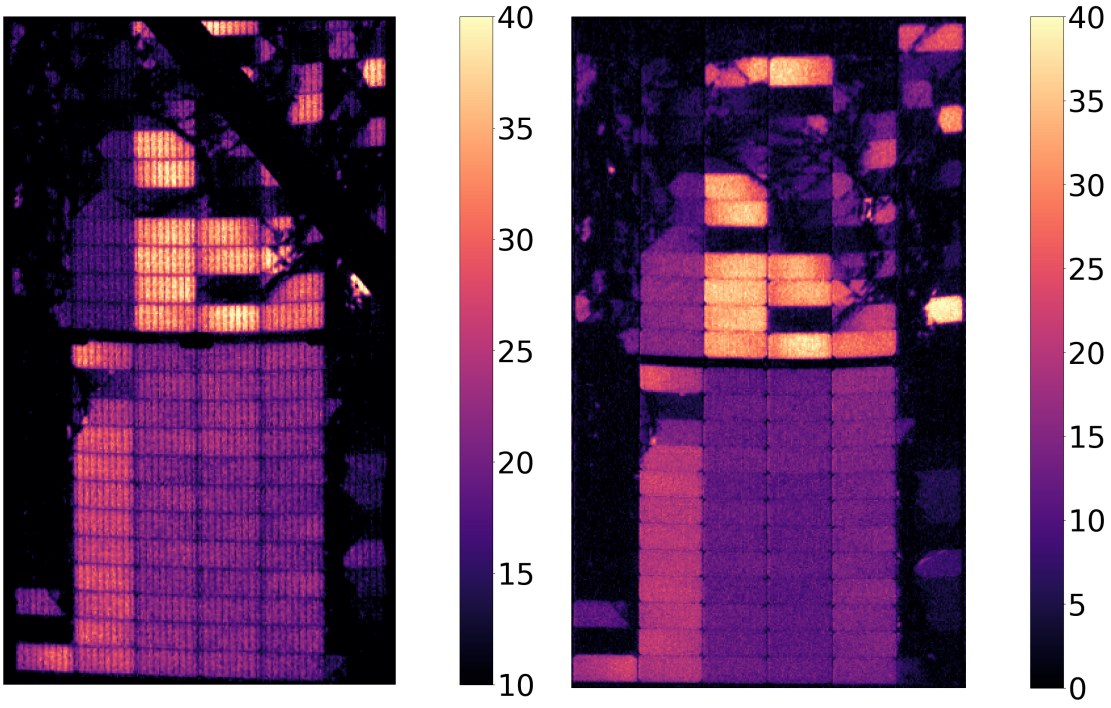

(a) Rear image of PERC1 in diffuse irradiance **(b)** Front image of PERC1 in diffuse irradiance

Figure 4.1.7: Comparison of dPL image of PERC1 in diffuse sunlight from (a) rear side and (b) front side.

The current level in Figure 4.1.8a and Figure 4.1.8b are in the same range but the current is slightly lower when the front images were captured than when the rear images were captured. The irradiance measured in diffuse conditions from the rear was 40 W/m^2. This is an average of the irradiance during the I-V curve sweep. For the front image, the irradiance was 53 W/m^2. Other conditions such as temperature may have had an effect on the current on the different days of measurement.

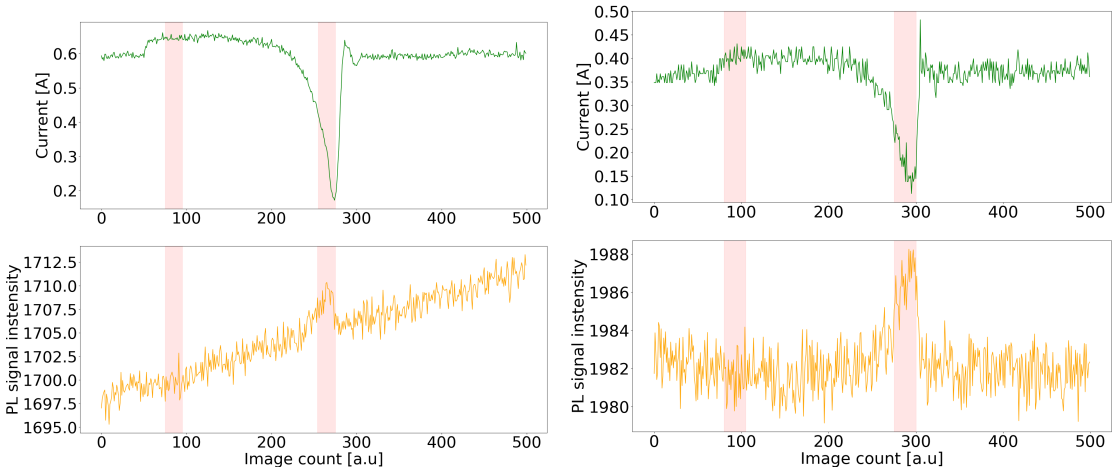

(a) Rear side of PERC1 in diffuse irradiance. **(b)** Front side of PERC1 in diffuse irradiance.

Figure 4.1.8: Comparison of the PL signal intensity and current of PERC1 in diffuse sunlight. Red areas represent the range of images used to produce the dPL image.

It is noticed that the PL signal intensity in Figure 4.1.8a is constantly increasing before and after the current drop. However, the current is constantly operating around MPP before and after the I-V curve sweep, so that one can assume that the irradiance is constant.

4.2 Rear Imaging in Direct vs Diffuse Irradiance

This section presents a comparative analysis between images obtained under direct irradiance and those acquired under diffuse irradiation. Additionally, this section includes a comparison of an image captured in diffuse irradiance with an EL image with 10% of I_{SC} applied, followed by a comparison of an image captured in direct irradiance with an EL image with I_{SC} applied.

dPL Images of PERC1

Figure 4.2.1 demonstrates the distinction between imaging from the rear under diffuse irradiance and under direct irradiance. The calculated SNR was 7.8 for the image in diffuse irradiance and 4.6 for the image in direct irradiance.

The images exhibit diverse cell information as the high intensity pixels are distributed spatially dissimilarly in the two images. Figure 4.2.1a shows that the two middle strings of cells in the lower half have a higher PL intensity than the rest, except for some of the cells on the upper half which partially have a high pixel intensity. The bus bars are more prominent in the image from direct irradiance but are quite visible in both.

The selections of images utilized for SC and OC in Figure 4.2.1a are illustrated in Figure 4.1.4a. Similarly, the images chosen for SC and OC in Figure 4.2.1b are illustrated in Figure 4.1.8a.

An observation made is that Figure 4.2.1b displays a greater number of cells that have become entirely dark, indicating low current flow or its absence through these regions. On the other hand, in Figure 4.2.1a, cells that have visible cracks show some observable current flow despite the damage. This particular detail is depicted in Figure 4.2.2, which is the area marked with green in Figure 4.2.1.

Figure 4.2.2 demonstrates that a cell with multiple cracks exhibits distinct characteristics under direct and diffuse irradiance. The region surrounding the crack in the cell appears to possess a current flow that is comparable to the surrounding cells in the direct irradiance image. Conversely, in the diffuse irradiance image, the same cell appears darker in comparison to the surrounding cells, indicating that the cell has a lower current flow than the others. Nevertheless, the comparison between the two images is challenging due to the differences in PL signal intensity and extracted currents, making direct comparison infeasible.

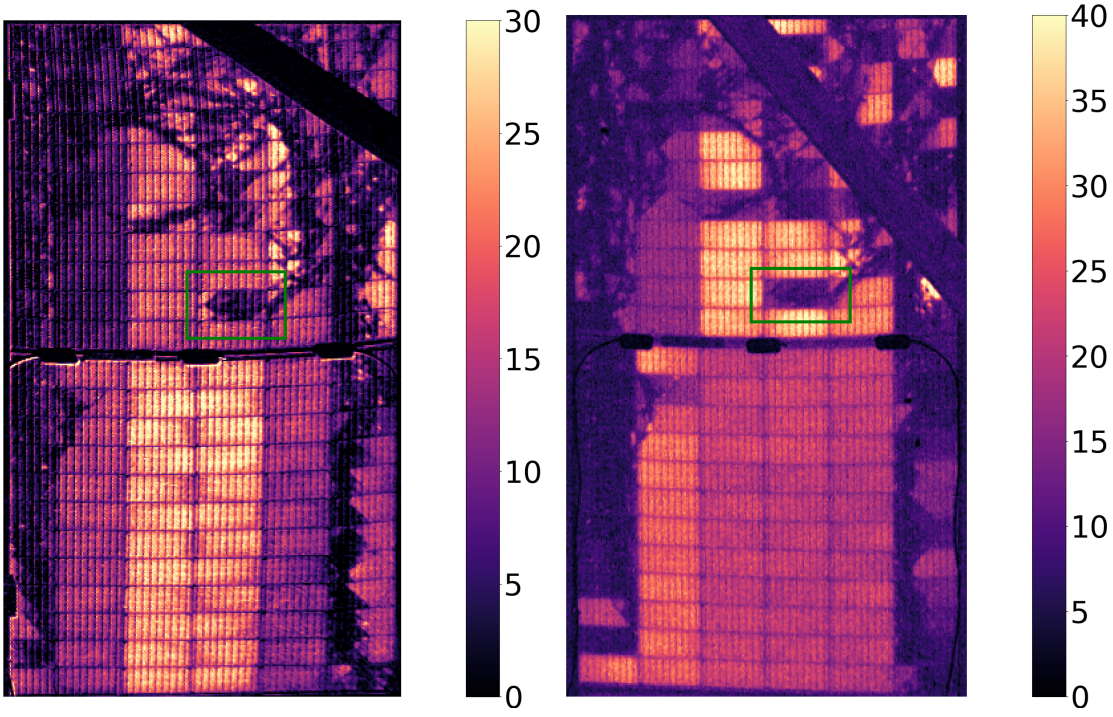

(a) Direct irradiance. **(b)** Diffuse irradiance.

Figure 4.2.1: Rear dPL image of PERC1.

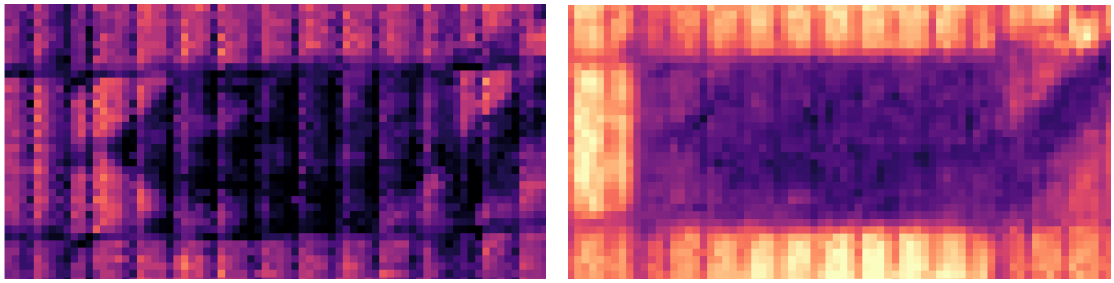

(a) Patch: Rear dPL image of PERC1 in direct irradiance. **(b)** Patch: Rear dPL image of PERC1 in diffuse irradiance.

Figure 4.2.2: Patches with details from the rear dPL image of PERC1 in direct and diffuse irradiance.

EL Images of PERC1

The EL images utilized in this study were obtained from a previous investigation where I_{SC} and 10% of I_{SC} were applied to the PERC modules. In Figure 4.2.3, the distinction between EL images obtained with the application of I_{SC} and 10% of I_{SC} is demonstrated. 20 images in each operation point are included in the EL images.

The difference in applied current results in a variation in EL intensity, which is represented by a distinct color scale in the images. Additionally, the images contain varied information, particularly in the upper half of Figure 4.2.3b, where several cells exhibit higher PL signal intensity in comparison to the surrounding cells. This pattern is akin to the observations made in Figure 4.2.1b obtained under diffuse irradiance.

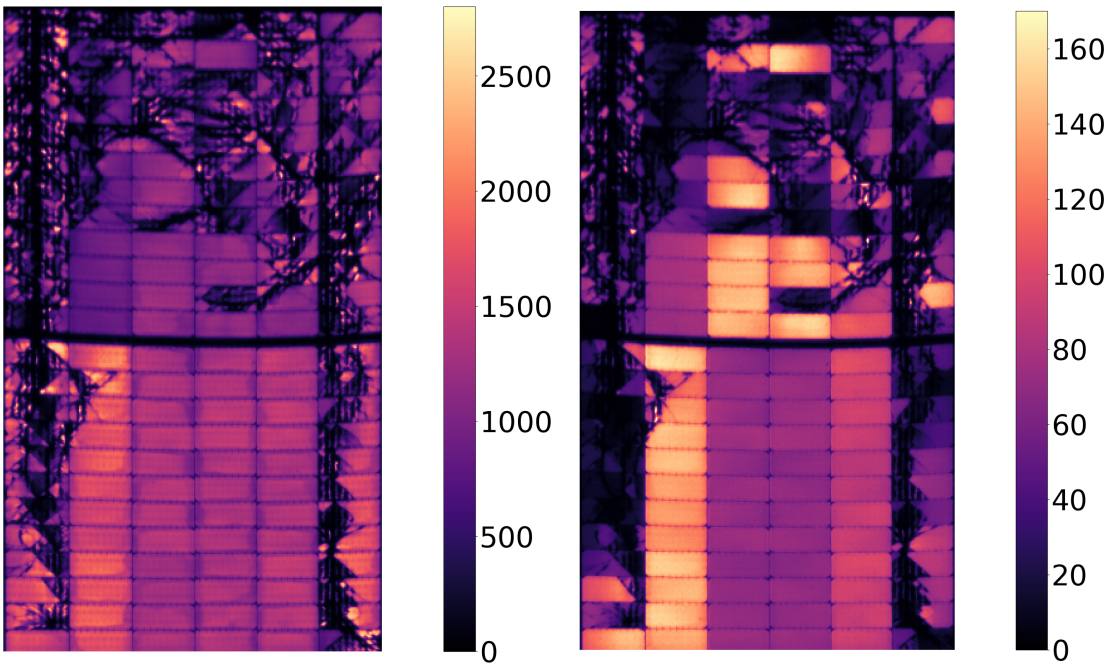

(a) I_{SC} applied. **(b)** 10% of I_{SC} applied.

Figure 4.2.3: EL images from the front side of PERC1.

Adjusted dPL in Diffuse Irradiance

The expected objective of Figure 4.2.1a was to produce a PL image from direct irradiance that closely resembled the I_{SC} EL image in Figure 4.2.3a. However, upon inspection, it was observed that the current flow patterns in the two images did not exhibit any obvious similarities. To address this issue, adjustments were made to the OC and SC image ranges for PERC1 in direct irradiance, in order to generate an image that more closely resembled the EL image with I_{SC} applied.

The image processing method for the modified image was the dPL algorithm, and the PL signal intensity and extracted current for the new ranges are plotted in Figure 4.2.4b. While the OC and SC range for Figure 4.2.1a were selected to maximize the difference in PL signal intensity, the ranges for the modified image were chosen to be closer to each other. This resulted in the final image shown in Figure 4.2.4a, where the green markers to the left and right indicate the SC and OC image ranges, both including 15 images.

It should be noted that the rear dPL image in Figure 4.2.4a exhibits a greater level of noise compared to the front EL image. Nonetheless, the current flow pattern in the dPL image more closely resembles that of the EL image in Figure 4.2.3a.

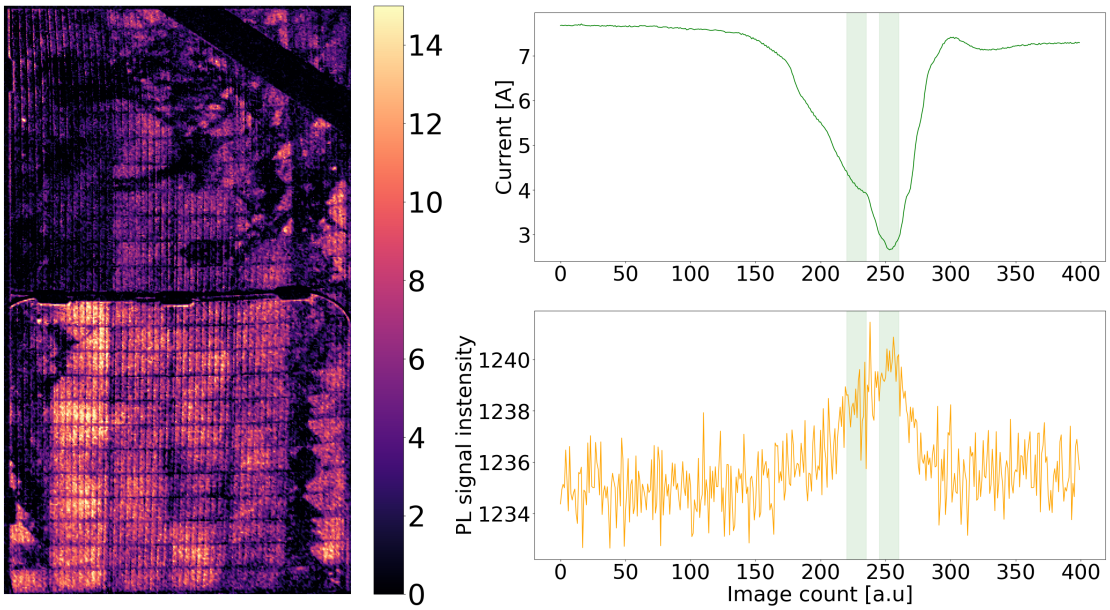

(a) dPL image of PERC1 in direct irradiance.

(b) Current and PL intensity graph with the adjusted images ranges marked in green.

Figure 4.2.4: dPL image of PERC1 in direct irradiance with adjusted image ranges for OC and SC.

4.3 dPL vs PCC Algorithm

This section will show a comparison of images that are processed and obtained using the dPL equation and images obtained using the PCC algorithm. The images and the corresponding current and PL signal intensity graphs will be presented. Normalized cumulative histograms are plotted in order to quantify the differences between the two images.

PERC3 in Direct Irradiance

Figure 4.3.1 shows a comparison of PERC3 in direct irradiance. The image processing method that is used to obtain Figure 4.3.1a is dPL, and the method that is used to obtain Figure 4.3.1b is PCC. The range of the color bar in Figure 4.3.1a is representing the pixel intensity in the dPL image. The range of the color bar in Figure 4.3.1b is representing the correlation coefficient, ranging from 0 to 1.

One can see that the PCC image has fewer background pixels with high intensity and that the module pixels are brighter and more uniform, while the dPL image has more variations in the module pixel's intensity and that several background pixels are with high intensity.

The color scale is set to range from 0 in both Figure 4.3.1a and Figure 4.3.1b, in order to emphasize that the background becomes darker in the PCC image. The color scale of the PCC image is further adjusted in order to entirely exclude the background and to emphasize the variations in the cell intensities within the module. This is shown in Figure 4.3.1c, where the color scale is ranging from 0.700 to 0.900.

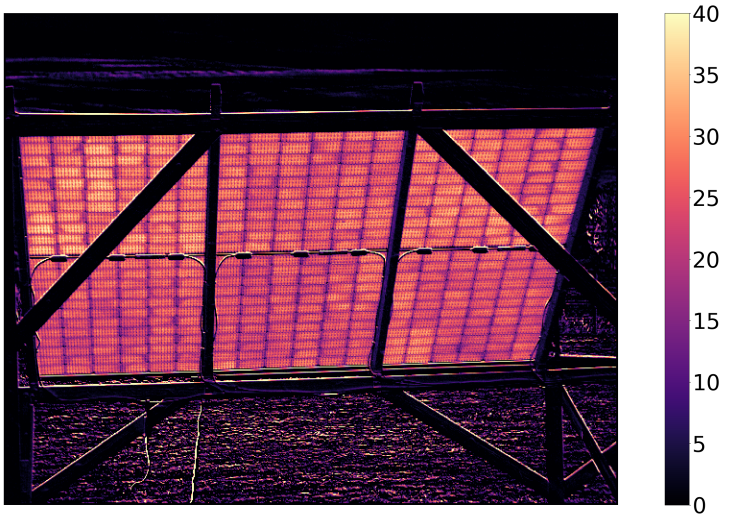

(a) dPL.

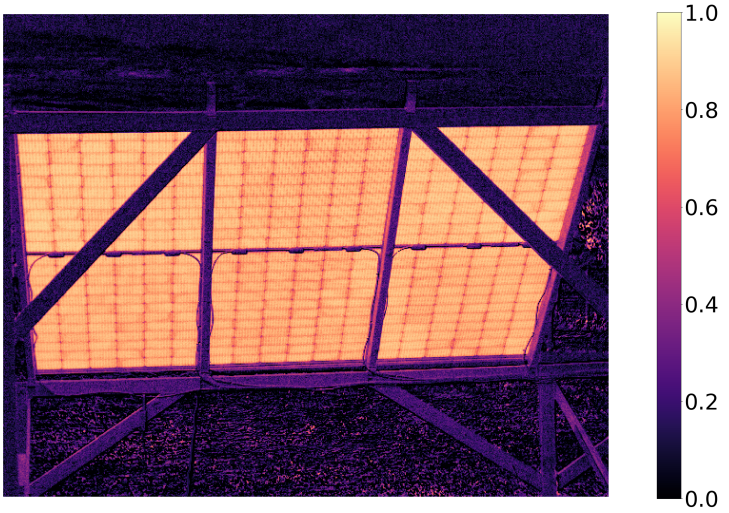

(b) PCC.

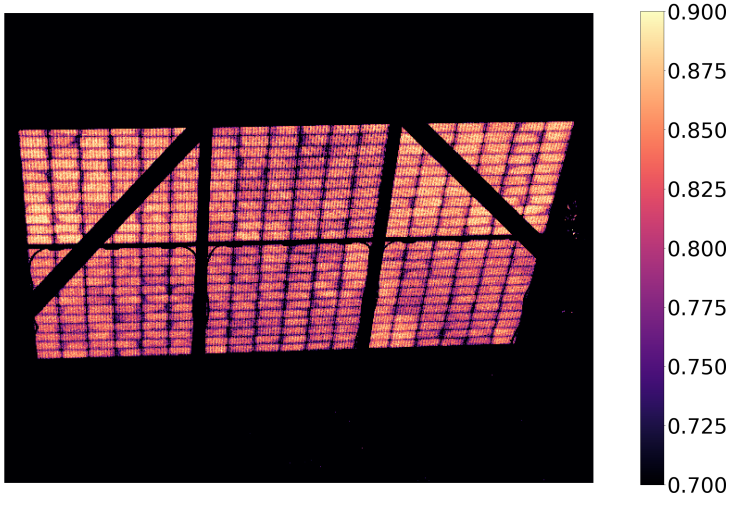

(c) Adjusted PCC.

Figure 4.3.1: PERC3 from the rear in direct irradiance.

The range of images that constitutes the SC and OC image in the dPL image is marked with red in Figure 4.1.2a. The range of images N that is applied to the PCC algorithm is marked with blue in Figure 4.3.2. 200 images around the current drop are selected in order to include the shape of the increased PL signal intensity.

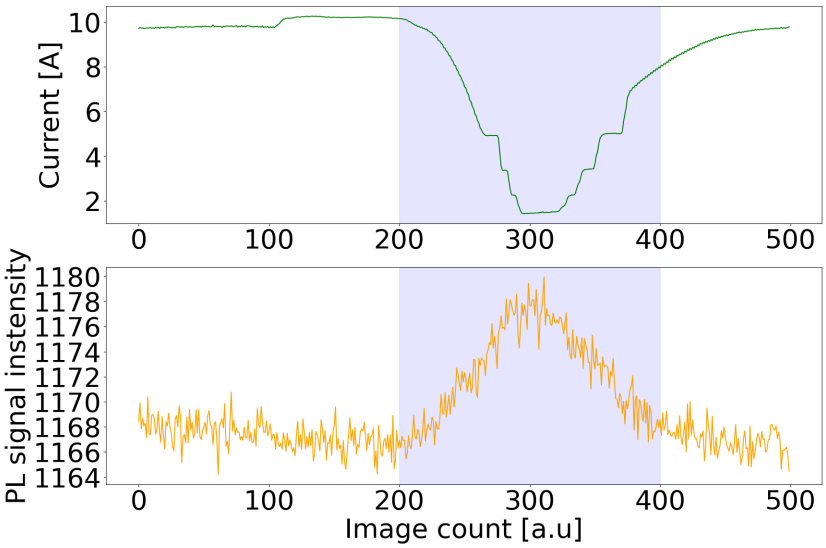

Figure 4.3.2: Image range N for the PCC image.

In order to quantify the differences between the dPL and PCC images, the normalized cumulative histograms were plotted and are shown in Figure 4.3.3. The intensity distributions of the pixels in the two images were found to be different based on the shapes of their respective histograms. Figure 4.3.3a illustrates that the dPL image has a steeper curve than the PCC image in Figure 4.3.3b.

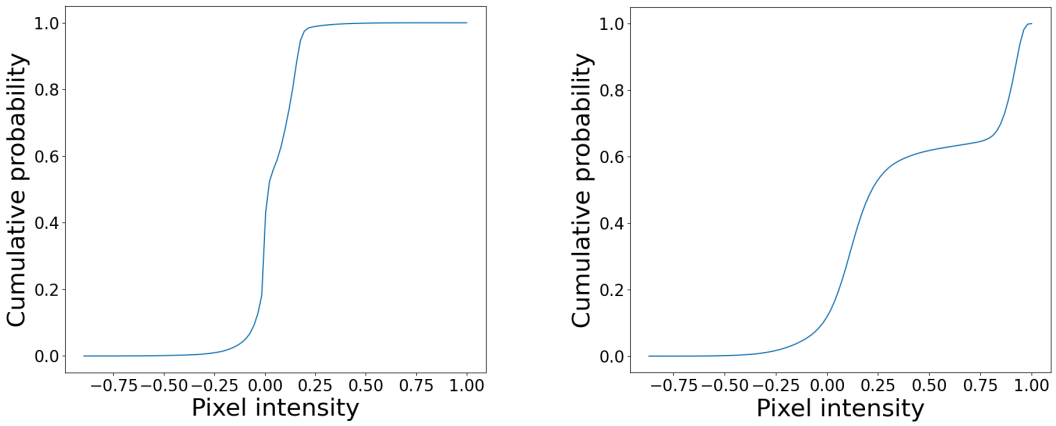

(a) Histogram of the dPL image.

(b) Histogram of the PCC image.

Figure 4.3.3: Normalised cumulative histograms of PERC3 from the rear in direct irradiance.

PERC3 in Diffuse Irradiance

Figure 4.3.4 shows a comparison of PERC3 in diffuse irradiance. The image in Figure 4.3.4a is processed with the dPL algorithm and Figure 4.3.4b is processed with the PCC algorithm.

Figure 4.3.4 exhibits the difference in pixel intensities of the background pixels, particularly the background above the modules. The color scale is set to range from 0 in both Figure 4.3.4a and Figure 4.3.4b, in order to show that the background becomes darker in the PCC image. The color scale of the PCC image is further adjusted in order to entirely exclude the background and to emphasize the variations in the cell intensities within the module. This is shown in Figure 4.3.4c.

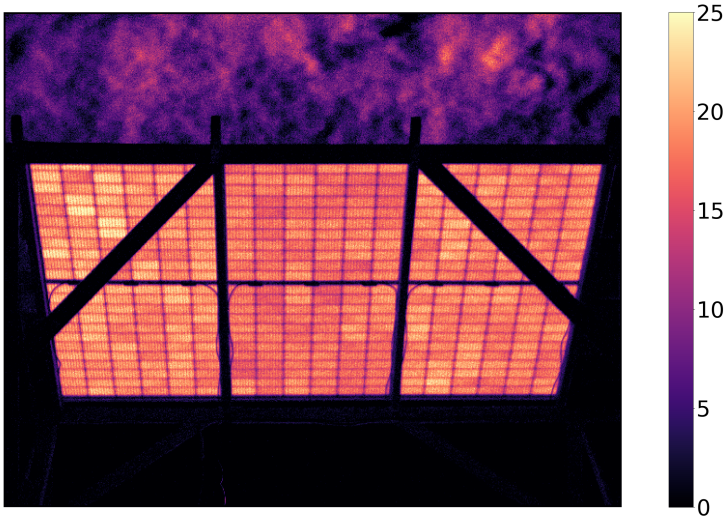

(a) dPL.

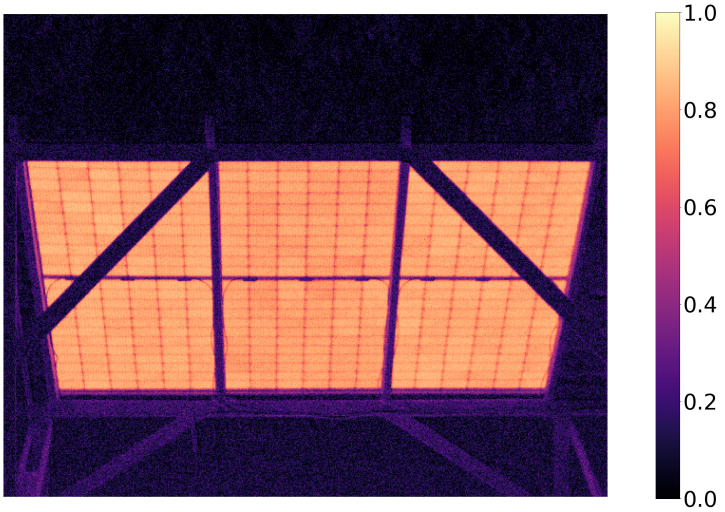

(b) PCC.

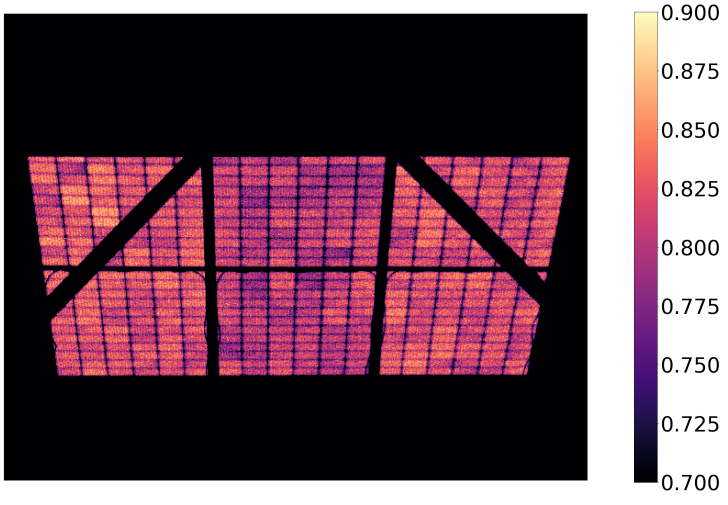

(c) Adjusted PCC.

Figure 4.3.4: Rear images of PERC3 in diffuse irradiance.

The ranges of images that constitute the SC and OC operating points in the dPL image are marked with red in Figure 4.1.6a. The range of images, N, that is applied to the PCC algorithm is marked with blue in Figure 4.3.5. In order to include the entire shape of the PL signal intensity increase, 140 images are selected to constitute N.

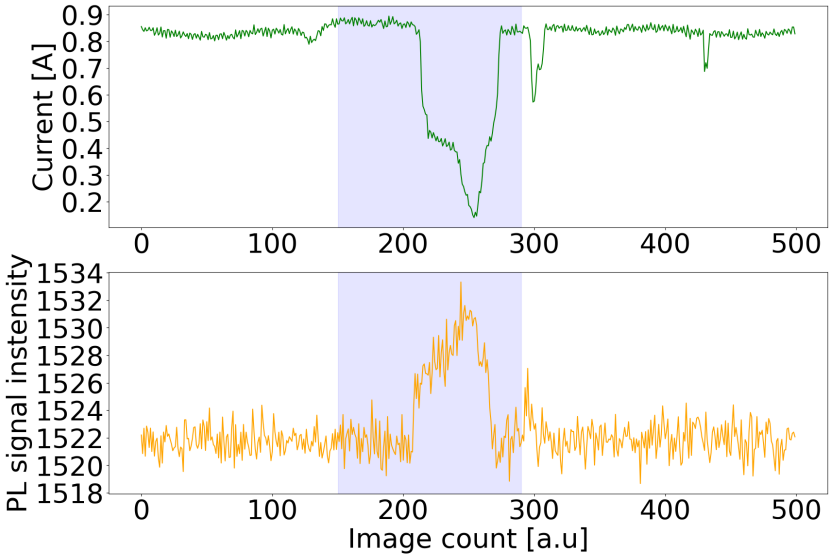

Figure 4.3.5: PCC image range (N) for PERC3 from the rear in diffuse irradiance.

The normalized cumulative histograms are plotted in Figure 4.3.6. The shapes are similar to the histograms from direct irradiance, and show the different intensity distribution of a dPL image and a PCC image.

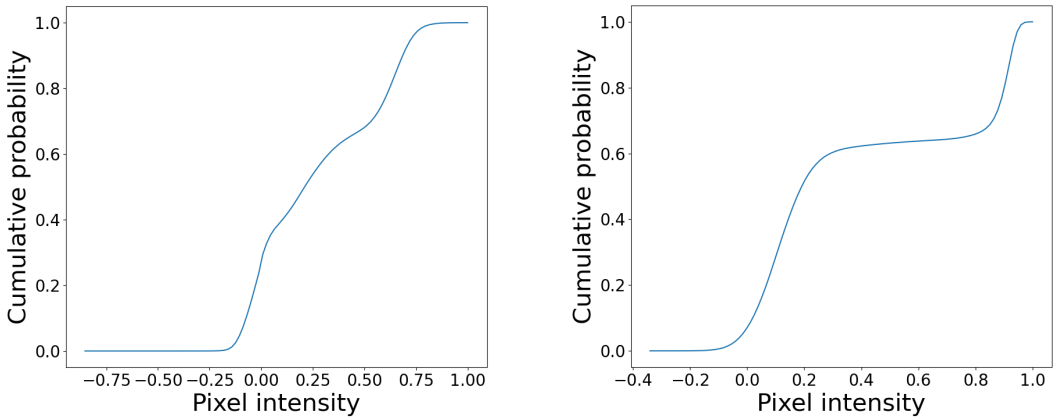

(a) Histogram of the dPL image.

(b) Histogram of the PCC image.

Figure 4.3.6: Normalised cumulative histograms of PERC3 from the rear in diffuse irradiance.

4.4 Smoothed vs Non-Smoothed PCC Images

In this section, the Savitzky-Golay smoothing filter is applied to the reference signal in the PCC algorithm. The PCC images are shown before and after the filter is applied. The Pearson correlation coefficient of the image is calculated in order to demonstrate the effect that the filter may have on the image.

PERC1 is chosen to be compared in this section, as the changes appear more visible on the damaged area than on healthy cells.

PERC1 in Direct Irradiance

Figure 4.4.1 shows different intensities from PERC1 in direct irradiance conditions. The green graph illustrates the intensity on one arbitrary background pixel, the blue graph illustrates one arbitrary module pixel, the yellow graph illustrates the mean image intensity (hereby referred to as the reference signal) before it is smoothed, and the red graph illustrates the smoothed reference signal. It is observed that the module pixel has a somewhat similar pattern to the reference signal, but the values of the reference signal are highly affected by both the module and the background pixels.

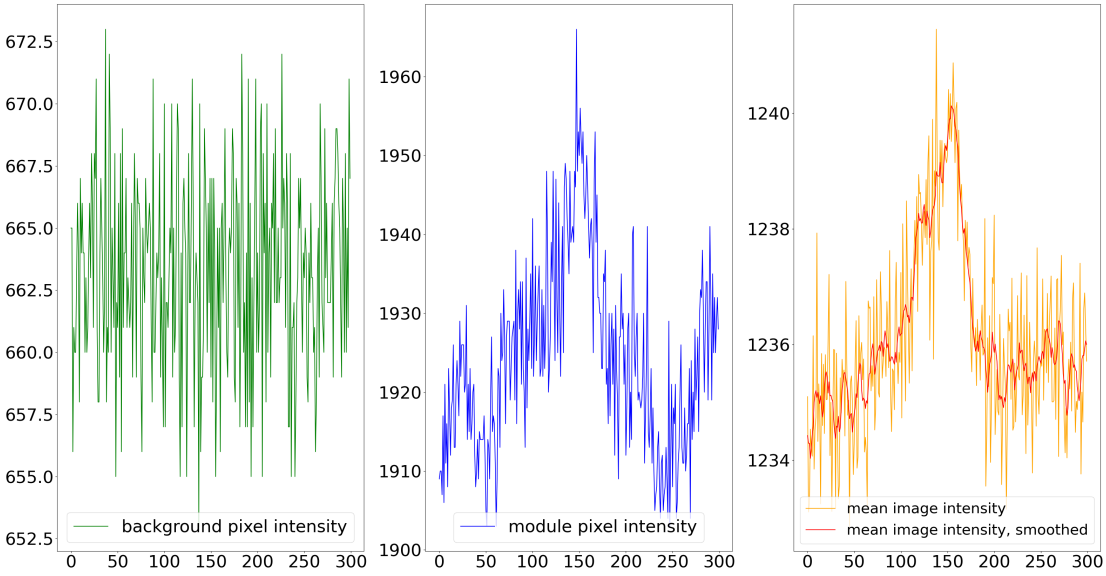

Figure 4.4.1: Direct irradiance: Background pixel, module pixel and reference signal intensities

Figure 4.4.2 illustrates how the reference signal smoothing affects the image. The background and the areas with damage are darker and the active cell pixels are brighter after the smoothing is applied. This is better visualized in the details in Figure 4.4.3.

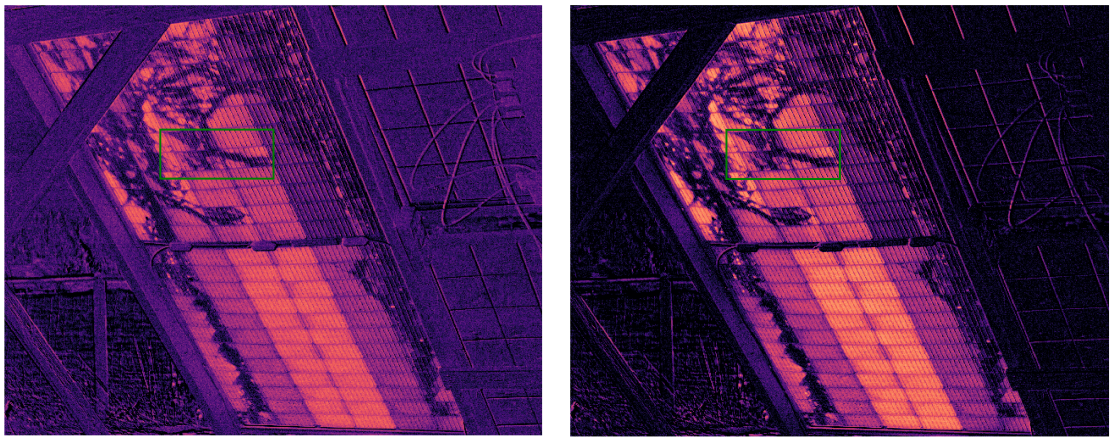

(a) PCC algorithm applied *without* smoothing. **(b)** PCC algorithm applied *with* smoothing.

Figure 4.4.2: Comparison of smoothed vs non-smoothed PCC image of PERC1 in direct irradiance.

.

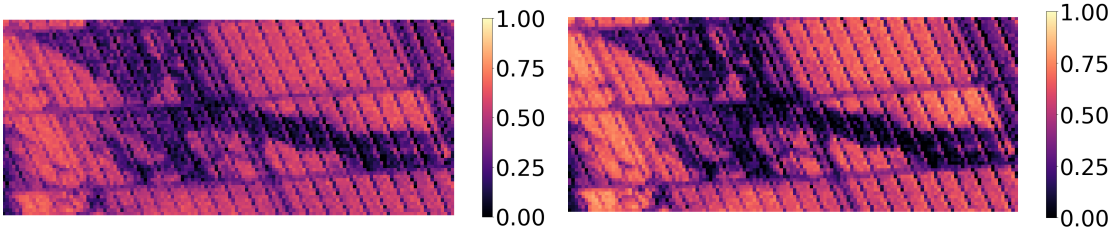

(a) PCC algorithm applied *without* smoothing. **(b)** PCC algorithm applied *with* smoothing.

Figure 4.4.3: Patch: Comparison of smoothed vs non-smoothed PCC image of PERC1 in direct irradiance.

Scatter plots and regression lines are plotted in order to visualize and quantify the differences that the smoothing makes. Figure 4.4.4 illustrates the change in correlation between the module and reference, and the background and reference, respectively

It is observed that for the module pixel, the scatter in Figure 4.4.4b is more collected than in Figure 4.4.4a, hence the correlation coefficient increases from 0.50 to 0.60. For the background pixel in Figure 4.4.4c, the scatter becomes more spread after the smoothing and hence the correlation coefficient decreases from 0.28 to 0.09. The correlation coefficients are summarised in Table B.1 in Appendix B.

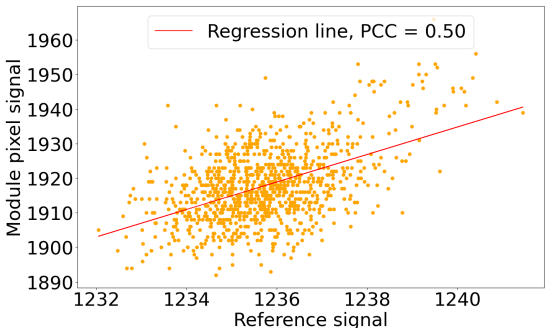

(a) Module pixel without smoothing

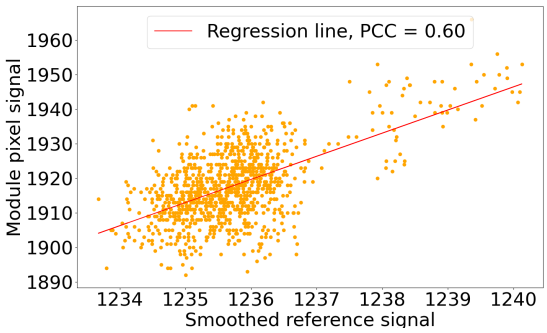

(b) Module pixel with smoothing

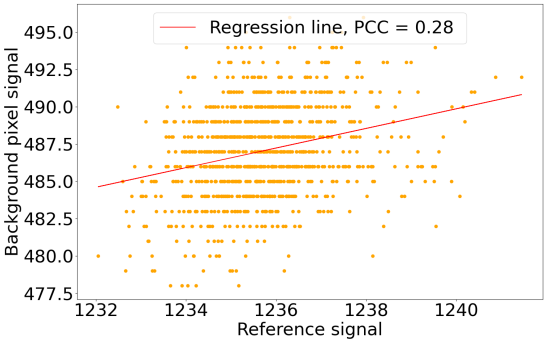

(c) Background pixel without smoothing

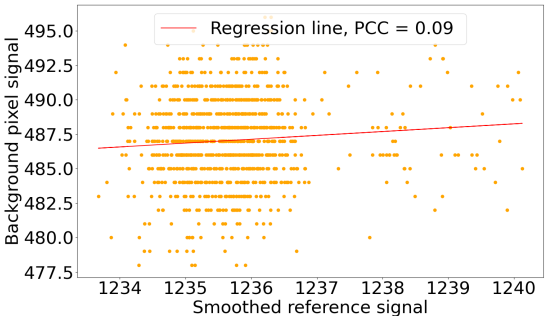

(d) Background pixel with smoothing

Figure 4.4.4: Scatter plots and regression lines of module pixel and background pixel before and after smoothing. PERC1 in direct irradiance.

PERC1 in Diffuse Irradiance

Figure 4.4.5 shows different intensities from PERC1 in direct irradiance conditions. The green graph illustrates the intensity on one arbitrary background pixel, the blue graph illustrates one arbitrary module pixel, the yellow graph illustrates the reference signal before it is smoothed, and the red graph illustrates the smoothed reference signal.

It is observed that the module pixel has a somewhat similar pattern to the reference signal in this case as well and that the values of the reference signal are highly affected by both module and background pixels.

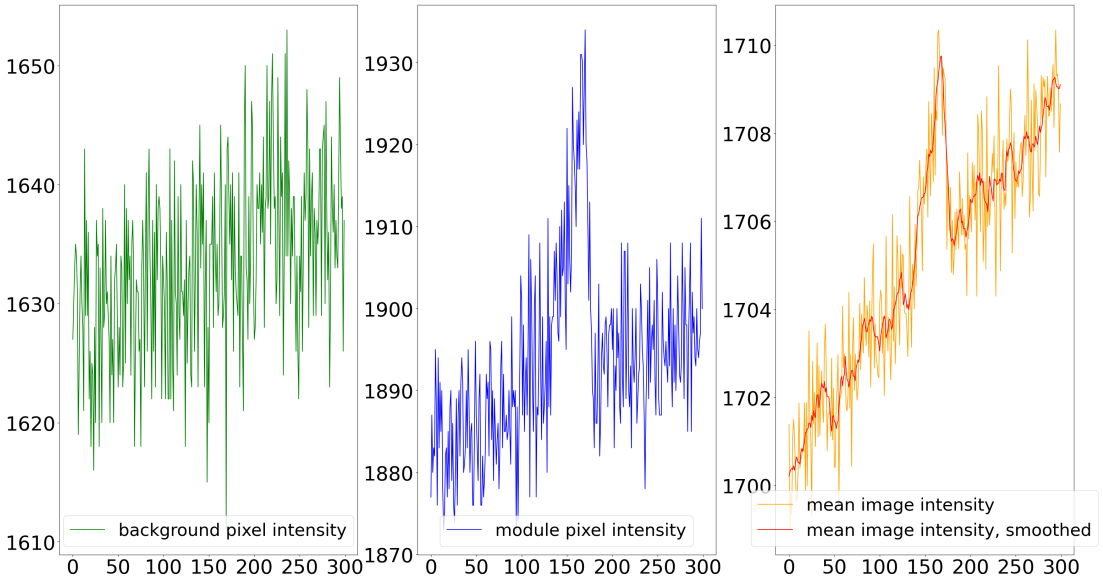

Figure 4.4.5: Diffuse irradiance: Background pixel, module pixel and reference signal intensities.

Figure 4.4.6 illustrates the effect of smoothing the reference signal in the diffuse condition image. The background is darker and the active cell areas are more prominent with a higher intensity value after the smoothing than before the smoothing. The color scale is shown in the detailed images in Figure 4.4.7, which are equivalent to their corresponding image.

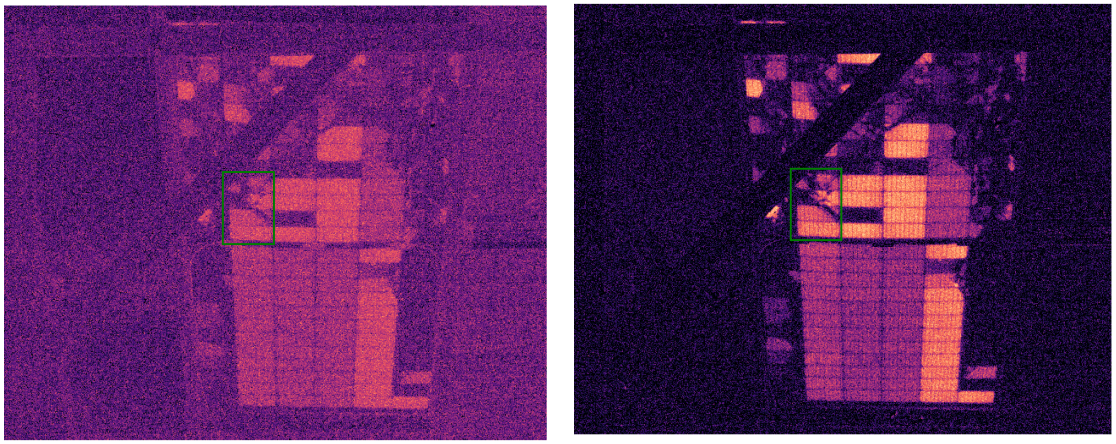

(a) PCC algorithm applied *without* smoothing. **(b)** PCC algorithm applied *with* smoothing.

Figure 4.4.6: Comparison of smoothed vs non-smoothed PCC image of PERC1 in diffuse irradiance.

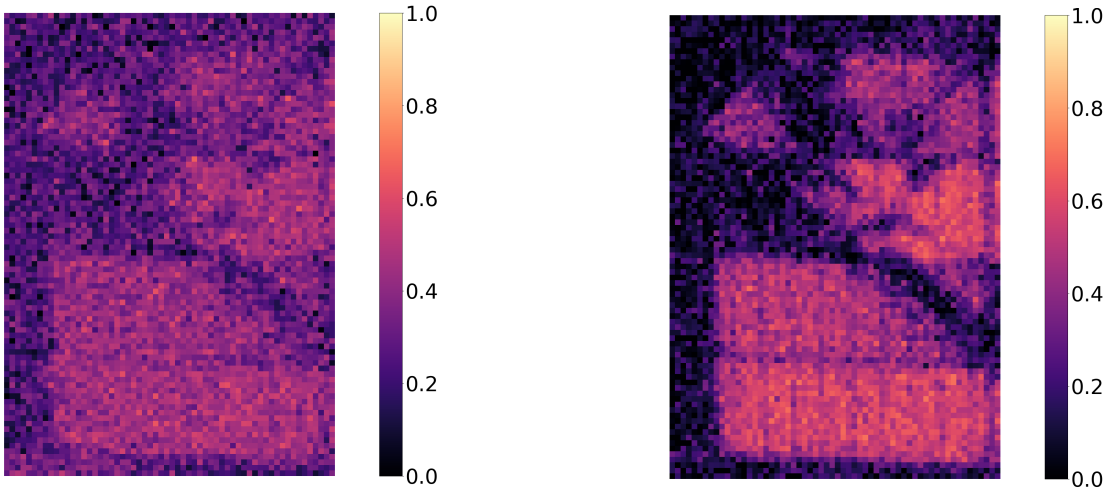

(a) Patch: PCC algorithm applied *without* smoothing.

(b) Patch: PCC algorithm applied *with* smoothing.

Figure 4.4.7: Patch: Comparison of smoothed vs non-smoothed PCC image of PERC1 in diffuse irradiance.

Figure 4.4.8d illustrates the change in correlation between the module and reference and the background and reference, respectively. It is observed that the correlation coefficient for the module pixel remains unchanged at 0.84 and that the scatter plots are slightly different but all scatter points are relatively close to the regression line. The background pixel becomes slightly affected by the smoothing, and the correlation coefficient decreases from 0.27 to 0.25.

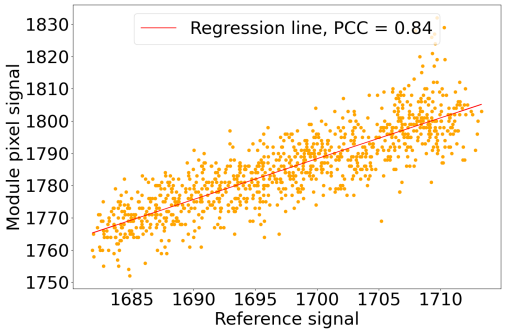

(a) Module pixel without smoothing.

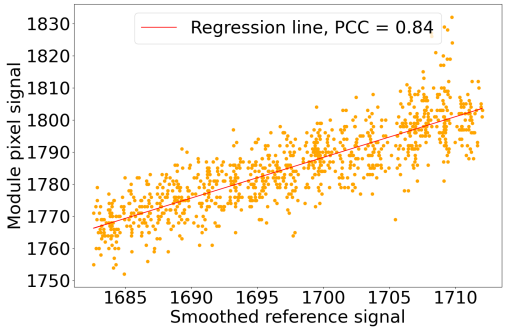

(b) Module pixel with smoothing

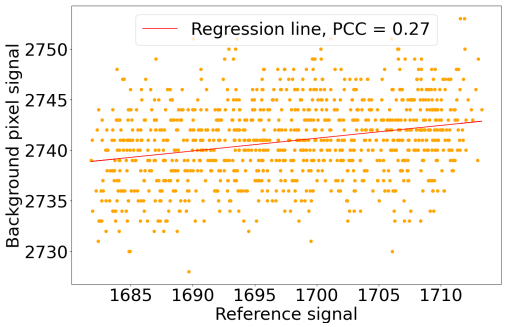

(c) Background pixel without smoothing.

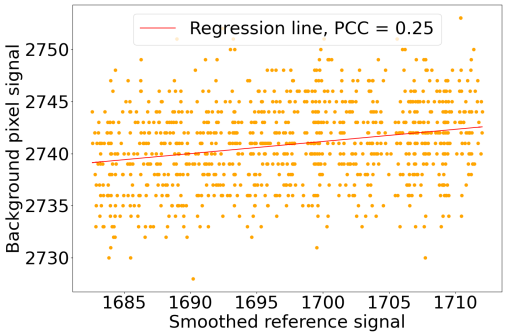

(d) Background pixel with smoothing.

Figure 4.4.8: Scatter plots and regression lines of module pixel and background pixel before and after smoothing. PERC1 in diffuse irradiance.

CHAPTER

FIVE

DISCUSSION

This chapter encompasses an interpretation of the results presented in Chapter 4, with the primary objective of addressing the research questions presented in Chapter 1. Furthermore, uncertainties pertaining to data collection and processing are addressed and discussed.

5.1 Interpretation

This section analyses the results as sectioned in Chapter 4. Section 5.1.1 comprises an analysis of Section 4.1 and assesses rear imaging as an alternative method of image acquisition. Section 5.1.2 analyses the potential and limitation of image acquirement in diffuse irradiance. Section 5.1.3 will discuss the benefits of the PCC algorithm and the last section will interpret the results from smoothing the PCC images.

5.1.1 Front vs Rear Imaging

It has been shown that it is possible to achieve a signal-to-noise ratio greater than 5 (up to 7.8), as calculated and presented in Table C.1 in Appendix C. This indicates that rear imaging can yield analysable results according to the technical specification of EL imaging and analysis. It is also proven in Figures 4.1.1-4.1.8 that the PL signals from the rear were of sufficient magnitude to generate an image that resembled the images obtained from the front side of the module.

According to the results in section 4.1, and the encounters that occurred during the experiments, PL imaging from the rear of a solar module has both advantages and disadvantages. One advantage is that diagnosing PV modules using PL becomes more flexible with the opportunity to image from the rear in addition to front imaging and opens new avenues to monitoring and inspection

of PV modules. Additionally, it might be advantageous in certain situations that rear imaging will not cause shadowing on the PV module.

As observed in Figure 4.1.1 the images display slightly different information. Most cells in Figure 4.1.1 show the same pattern in extracted current (only the intensity scale is different). However, some cells such as the one in the top right corner in Figure 4.1.1a seem to be discrepant from the corresponding cell in Figure 4.1.1b, meaning that rear images might complement the front imaging when diagnosing and analysing damages of a PV module. In a bifacial module, the rear and front sides might degrade at different rates, due to the difference in exposure to environmental factors such as snow, hail, pollutants and partial shadowing from leaves, trees and other circumstantial elements. To obtain a comprehensive understanding of what affects the efficiency of the solar cell module and what the diagnosis may be, it may be necessary to capture images from both sides.

The results demonstrate that all rear images of the PV modules have more prominent bus bars than the images from the front.

When visually inspecting the images, bus bars may complicate the identification of cracks and bus bars as they both appear dark. However, the development of computer vision technologies will enable tracking defects in different types of technologies in order to improve the efficiency and reliability that lacks in manual surface defects inspection [36]. The technology is further developed in order to detect bus bar defects such as scratches, hole spots and broken fingers/bus bars [37]. The deep convolutional neural network (CNN) method is based on image analysis of the bus bars whereas the rest of the cell (background) is color masked and excluded in order to analyse the bus bars and detect surface defects. It can be a great opportunity for technologies such as CNN to image from the rear as the bus bars are more visible and the distinction is more facile. Assessing the bus bars and identifying damages using CNN from rear imaging is a task that would have been interesting to explore in future work, but is beyond the scope of this thesis.

However, there are some restrictions and disadvantages to the method that one should be aware of when imaging from the rear of the PV modules, which are divided into practical challenges and challenges in the analysis.

First of all, an obvious challenge is how the modules are mounted on poles that will somehow cover some of the cells regardless of the angle when imaging from the rear. The mounting might be different in other power plants, but in this case, there is one pole at the top that covers the top one or one and a half rows of cells of the PV modules. This inhibition is constant throughout all rear images in these experiments. In addition to the top pole, there are diagonal poles that cover several cells. It is possible to adjust the angle of the camera when capturing the

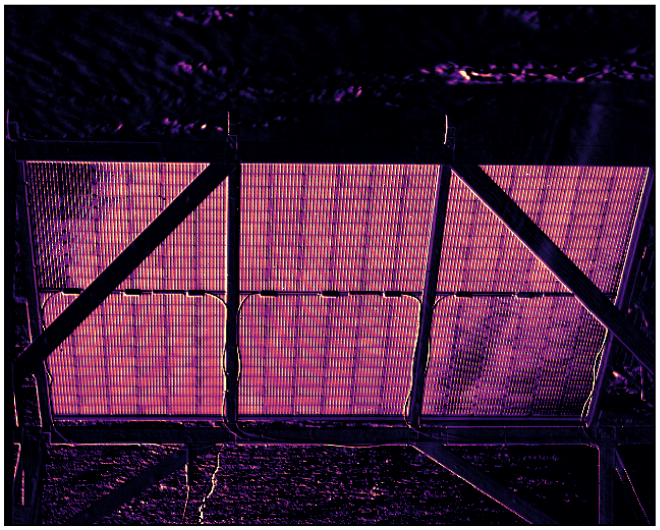

Figure 5.1.1: The unwanted effects appeared as circular lines on the module, and two corners were shaded.

images so that the diagonal pole covers different cells in the PV module. However, there will always be some degree of obstruction present if the image is captured at an angle that also shall render analyzable solar cells. Although this inhibition was unavoidable in these experiments, it is conceivable that the mounting of bifacial PV modules is conducted in a different way in order to exploit diagnosis from the rear in a setting with a larger scale.

One issue that will make large-scale rear monitoring of PV modules strenuous, pertains to the angle at which the modules are mounted relative to the ground. Large-scale imaging of solar power plants requires a large distance which is not feasible at the angle that most modules are mounted. The angle that can be achieved when capturing images of the module using aerial inspections, results in less distortion when applying perspective transformation during image processing. However, the row of solar cell modules positioned behind will limit the distance that can be achieved in the image when approaching from the rear. Nevertheless, if there were enough space behind the module row, the angle would still be non-optimal and result in great distortion of the perspective transformed images in the image processing.

The third concern regarding the angle of the rear PL image capturing is the sun's position. In direct sunlight conditions, the sun radiated directly on the PV modules but also on the camera lens in the rear of the modules, as Figure 3.1.6 illustrated. The effect that appeared on the discarded images is shown in Figure 5.1.1. This practical issue will propagate to an analysis issue if it is not taken into account in the data collection.

The last concern that was elucidated through the practical part of these

experiments is the risk of saturated images. The rapid change of the sun's position constitutes a risk of saturating parts of the image that shall be analyzed. This means a risk of losing information on the pixel intensities in certain pixels and how they are distributed in the saturated area. It is therefore important to also consider the direct sunlight for the whole period that the imaging will take place. In this case, the imaging procedure had a duration of over 20 minutes and the sunlight was therefore not a problem initially, but after a while the exposure changed and the saturation would disturb the images. In general, it is important to measure the irradiance due to sudden movements in the clouds or their change in opacity, which can affect the irradiance. This accounts for front imaging as well.

As for the analytical part of the interpretation, there are a few elements to be aware of. The information obtained from the graphs and images of the front and back of the module is not directly comparable due to the higher proportion of incoming irradiance received by the front. The irradiance received by the rear side is dependent on ground-reflected irradiance (Albedo) and diffuse/scattered irradiance, e.g. from the surrounding clouds or buildings. Based on this information, it can be assumed that the PL signal intensities from the front and back will be closer to each other under diffuse irradiance than under direct irradiance, as a higher proportion of the incoming radiation will be impinging the rear side. Although the front and rear imaging might be more comparable under diffuse than direct irradiance, the PL signal is still much weaker, which can make defect detection more challenging.

5.1.2 Rear Imaging in Direct vs Diffuse Irradiance

It has been investigated whether it is possible to achieve a respectable SNR value from the back of solar cell modules under diffuse and direct irradiance, and the results showed that it was possible to obtain an SNR of up to 7.8 from the rear under diffuse irradiance, and 6.9 from the rear under direct irradiance. This means that the signal is strong enough to obtain analyzable images from the rear in diffuse irradiance, although it has been shown in Figure 4.1.6 and in Figure 4.1.8 that the PL signal is consistently weaker in diffuse irradiance than in direct irradiance. However, as discussed in the previous section, it is not necessary to have a strong PL signal in order to generate an image that resembles the front images.

Achieving a signal with a sufficient SNR under diffuse irradiance presents several advantages for rear-side image acquisition. One advantage is the ability to take pictures head-on, unlike in direct sunlight where consideration must be given to sunlight in the camera lens. The effects discussed in the previous section and shown in Figure 5.1.1, which was also a problem although a camera lens hood

was attached, can be avoided in diffuse conditions. Taking pictures head-on also avoids distorting images during perspective transformation, resulting in images that are closer to the "true" images since they are manipulated to a lesser extent.

Regarding the analysis of the images, the information obtained depended on the desired outcome, as both diffuse and direct irradiance has shown to provide different information about the modules. It has been observed that the EL images captured with 10% of I_{SC} in Figure 4.2.3b has similarities and are comparable to the PL images captured in diffuse irradiance in Figure 4.2.1b. Moreover, it was found that after some experimentation with the selection of OC and SC, an image resembling the EL image at I_{SC} in Figure 4.2.3a can also be obtained. This was shown in Figure 4.2.4a. The image appears to have slightly lower quality compared to the EL image, possibly due to the reduced number of images selected. However, it is noteworthy that the image bears similarities to the EL image with $_{SC}$ applied, particularly in terms of current flow.

Capturing images in both direct and diffuse irradiance can greatly enhance the capabilities of diagnosing PV modules. EL imaging has been shown to detect different types of cracks/degradation modes (DM) through the different current levels I_{SC} and 10% of I_{SC} [38]. In order to identify these types of cracks through different current levels, imaging under both diffuse (100 W) and direct (1000 W) irradiance has been shown to correlate to the two different current levels [21], which is also shown in this thesis. Identifying and categorizing different DM is a task that would have been interesting to explore in future work, but is beyond the scope of this thesis.

In general, imaging under diffuse irradiance cannot replace or be equivalent to imaging under direct irradiance, as we have observed that they provide substantially different information about PV modules. However, the images obtained under diffuse irradiance can complement the images obtained under direct irradiance and provide more comprehensive diagnostic information.

5.1.3 dPL vs PCC Algorithm

In the dPL image in Figure 4.3.1, the background pixels exhibit high PL intensity values for some unknown reason. This may be attributed to either reflection from the module on the grass, which would have the same variation in PL signal as the module, or it could be due to random noise and fluctuations that result in radiative emission in the PL wavelength range.

The PCC method was utilized to eliminate the background noise by measuring the correlation between each pixel and the reference signal of the image. The PCC images in Figure 4.3.1b and Figure 4.3.4b show a reduction in background

intensity. The scale was set from zero to one in order to display the entire range of intensities. The background and poles did not have zero correlation with the reference signal, which may be due to the proportion of the module and the background in the image. This means that the background affects the reference signal enough for the background pixels to have some correlation with the reference signal.

Since the module appears relatively uniform in Figure 4.3.1b and Figure 4.3.4b, the scale was adjusted to show the variations in the module while completely excluding the background and poles. The result was shown in Figure 4.3.1c and Figure 4.3.4c, which resulted in the module cells corresponding to the distribution of pixel intensity as shown in Figure 4.3.1a and Figure 4.3.4a, but with better exclusion of the background. It is possible that this method also removes noise in front of the module that cannot be distinguished from the module in a dPL image, making the diagnosis more precise.

As shown in Figure 4.3.3, the plotted histograms of the dPL image and PCC image were of different characteristics. The shape of the PCC histogram in Figure 4.3.3b Figure 4.3.6b can be interpreted as the algorithm being better at distinguishing pixels with low intensity from those with high intensity. This can be seen in the "dump" in the graph for the middle range of pixel intensities. The fact that it does not increase here means that it does not count any pixels with a medium intensity. In the steep region, i.e. around 0.0-0.25, there are many counted pixels (about 60%) before it flattens out for intermediate intensity pixels. Where it becomes steep again (around 0.75-1.0), the remaining pixels are located. Thus, the algorithm counts about 60% of the pixels with values from 0.0-0.25 in intensity (dark pixels) and about 40% of the pixels with 0.75-1.0 (bright pixels).

In Figure 4.3.3a, this dump is less elongated and distinct. Thus, there is not a large range of intermediate and high intensity pixels, as almost all pixels are counted in the low intensity range (approximately 0.0-0.25), which is interpreted as the dPL algorithm not being able to clearly distinguish between dark and bright pixels, i.e. background and module pixels. Figure 4.3.6a illustrates that the pixels are evenly distributed between 0 and 1, also with a less elongated and distinct dump as in Figure 4.3.3a, meaning that the algorithm does not distinguish between module and background.

In addition to improving the accuracy of diagnostics, PCC can make the imaging process more efficient by eliminating the need for manual processing of the data after acquisition and before analysis. The method removes the manual selection of two operating points in the image series and instead enables the feeding of the entire data collection into the algorithm. This approach can speed up the completion of an exhaustive amount of processing, contributing to the streamlining

of PL-based diagnostics. Relative to the dPL algorithm, the PCC algorithm "will contribute to an efficient, unsupervised image processing and thus easier real-time implementation" [12].

5.1.4 SG smoothing effect on PCC images

Figure 4.4.1 and Figure 4.4.5 illustrated the impact of smoothing on the signal intensity. The plot clearly indicated a significant change in the signal intensity graph as a result of the smoothing with most of the outliers removed. It could be conjectured that the considerable effect of the module pixels on the initial graph would lead to a reduction in correlation between the module and the new reference graph. The observed increase in correlation suggests that the distinctive shape of the graph played a crucial role in the correlation increase. Additionally, it should be noted that the outliers did not have a huge impact. Specifically, for the background pixel graph, it can be inferred that only the outliers in the original reference graph were correlated, and when these outliers were removed by smoothing, the correlation would decrease.

In Figures 4.4.2 and Figure 4.4.6, as well as in the detailed images in Figure 4.4.3 and Figure 4.4.7, it can be observed that the dark pixels in the background and cracks become darker, while the active cells in the module have higher intensity as a result of smoothing. This is consistent with the results shown in the scatter plots in Figure 4.4.4 and Figure 4.4.8. Figure 4.4.4 and Figure 4.4.8 also demonstrate that the image in diffuse irradiance resulted in a higher correlation for the module and a lower correlation for the background than the image in direct irradiance.

The results demonstrate that the SG smoothing filter can enhance image clarity and highlight active cells, while providing contrast to the images, making it visually easier to distinguish between active and inactive parts of the cells.

5.2 Uncertainties and Limitations

Outdoor imaging is subject to sources of human measurement errors and uncertainties. These can include wind and unstable ground surfaces that lead to noisy, blurry and/or inaccurate images, as well as the sun's movement in the sky that can cause saturation in the image. These factors should be taken into consideration when capturing outdoor images. However, such factors are accounted for in an SNR analysis. If an SNR analysis is conducted in accordance with the EL imaging standard and meets the SNR requirements, the resulting images should be analyzable.

Perspective transformation is a source of uncertainty as it involves manipulations in the image. However, awareness of this manipulation makes it easier to perform a correct analysis. From a spatial perspective, it may cause a shift in the regions of interest, but it will not provide erroneous information regarding non-existent damages or extracted current.

In comparisons between front and rear as well as direct and diffuse images, the difference in irradiances is not corrected. The various irradiances have been measured and mentioned throughout the thesis, but the values of current and PL signal intensity are as measured on-site. Therefore, there may be inaccuracies in the analysis concerning irradiance.

It cannot be definitively stated whether direct or diffuse irradiance is better, as discussed in Section 5.1.4. The pixels selected for comparing the correlation between module/background and reference are randomly chosen and subject to variation, given the thousands of pixels available for selection.

Lastly, it is emphasized that the different SNR values are not the only values that can be obtained from a large range of images. There can be innumerable amount of combinations of image ranges resulting in different SNR values and different dPL images. An SNR of 1.5 does not necessarily mean that there is no existing range of images that can be selected to obtain a greater value. The table of SNR values serves as a guideline for good-quality images according to the EL standard. For images with SNR lower than 5, it is recommended to keep in mind the SNR when analyzing the image.

CHAPTER

SIX

CONCLUSIONS

Although rear imaging offers certain advantages, it also poses practical and analytical challenges that must be carefully considered when using this technique. Solutions need to be developed to overcome these challenges in order for rear imaging to be beneficial. However, it presents an opportunity to increase flexibility and expand the PL diagnosis of PV modules. Several factors have been identified as causing lower PL signals at the rear side than at the front side, but it has been demonstrated that a high and strong signal is not necessary to generate images and analyze damages in a solar cell module, as many adjustments can be made in the image processing.

Overall, rear imaging may not replace large-scale imaging from the front side, but it can provide supplementary information about the module and further experimentation is warranted, particularly as the utilization of bifacial modules is progressively gaining momentum. This means that rear imaging contributes to increased flexibility and accuracy in the image diagnosis of PV modules.

Another possibility for increasing flexibility and expanding the PL method is imaging in diffuse irradiance. In this case too, it was observed a lower PL signal, but it was still a sufficient signal in order to analyze the image. Similarly, adjustments can be made in the image processing.

Through some experimentation and examination of the OC and SC image ranges, it was found that dPL images can provide the same patterns as EL images in I_{SC} and $I_{0.1SC}$. As discussed, this could open some new avenues in the analysis as images in different current/irradiation conditions can be used to categorize different defect modes.

Overall, imaging in diffused irradiance can not replace imaging in direct irradiance, as we have observed that they provide completely different information, but they can complement the method and provide supplementary information

about the PV modules. This means that imaging in diffuse irradiance contributes to increased flexibility and accuracy in PL diagnosis.

The PCC algorithm has the potential to make PL imaging more efficient, as it does not need to be supervised and does not require manual pre-processing. Additionally, it has been observed that by being aware of the selected image range N included in the PCC algorithm, the method has the potential to make PL imaging more accurate as well.

The results showed that the algorithm is better at removing background noise and distinguishing between module pixels and background pixels. SG-smoothing was found to amplify these advantages by providing even less correlation to the background and a higher correlation to the module, in addition to enhancing the visual effect of the damages on the module in the images. Therefore, it can be concluded that the smoothing process contributed to increased accuracy in the PL images.

REFERENCES

[1] International Energy Agency, 2022. *World Energy Outlook 2022*. Accessed: 2023-29-03. 2022.

[2] International Energy Agency, 2022. *Renewable Energy Market Update - May 2022*. Accessed: 2023-18-04. 2022.

[3] International Energy Agency, 2019. *World Energy Outlook 2019*. Accessed: 2023-18-04. 2019.

[4] International Energy Agency, 2021. *Net Zero by 2050*. Accessed: 2023-18-04. 2021.

[5] A. Smets and K. Jäger et. al. *Solar Energy - The physics and engineering of photovoltaic conversion technologies and systems*. UIT Cambridge, 2016, p. 268.

[6] A. A. Aminou Moussavou, AK. Raji, and M. Adonis. "Impact study of partial shading phenomenon on solar PV module performance". In: *2018 International Conference on the Industrial and Commercial Use of Energy (ICUE)*. 2018, pp. 1–7.

[7] I. Høiaas. *Overview of defects and imaging techniques*. . Accessed: 2023-03-02. 2020.

[8] Raghavi Bhoopathy et al. "Outdoor photoluminescence imaging of photovoltaic modules with sunlight excitation". In: *Progress in Photovoltaics: Research and Applications* 26.1 (2018), pp. 69–73. DOI: 10.1002/pip.2946.

[9] T. Trupke et al. "Spatially resolved series resistance of silicon solar cells obtained from luminescence imaging". In: *Applied Physics Letters* 90.9 (2007). DOI: 10.1063/1.2709630.

[10] E. Kaplani. *Degradation in Field-aged Crystalline Silicon Photovoltaic Modules and Diagnosis using Electroluminescence Imaging*. Accessed: 2023-19-04. 2016.

[11] Iskra Zafirovska et al. “Module Inspection Using Line Scanning Photoluminescence Imaging”. In: July 2016. DOI: 10.4229/EUPVSEC20162016-5BV.1.12.

[12] M. Vukovic, K. H. Liland, and U. G. Indahl et. al. “Extraction of photoluminescence with Pearson correlation coefficient from images of field-installed photovoltaic modules”. In: *Submitted to* ().

[13] Benatto, G. A. D. R., Chi, M., Santamaria Lancia, A. A., Riedel, N. *Scaling up Laser Line Photoluminescence Imaging for Outdoor Inspections*. Accessed: 2023-19-04. 2018. DOI: 10.4229/35thEUPVSEC20182018-5CV.3.41.

[14] Oliver Kunz et. al. “Outdoor luminescence imaging of field-deployed PV modules”. In: *Progress in Energy* 4.4 (2022). DOI: 10.1088/2516-1083/ac9a33.

[15] Raghavi Bhoopathy et al. “Outdoor photoluminescence imaging of photovoltaic modules with sunlight excitation”. In: *Progress in Photovoltaics: Research and Applications* 26.1 (2018), pp. 69–73. DOI: 10.1002/pip.2946.

[16] Raghavi Bhoopathy et al. “Outdoor photoluminescence imaging of solar panels by contactless switching: Technical considerations and applications”. In: *Progress in Photovoltaics: Research and Applications* 28.3 (2020), pp. 217–228. DOI: 10.1002/pip.3216.

[17] I. E. Høiaas. *Hyperspectral imaging as a tool to study solar induced photoluminescence from PV modules*. 2019.

[18] M. Vukovic, I. E. Høiaas, and M. Jakovljevic et.al. “Photoluminescence imaging of silicon modules in a string”. In: *Progress in Photovoltaics* 30 (4 Jan. 2022), pp. 436–446. DOI: 10.1002/pip.3525.

[19] M. Vukovic, M. Jakovljevic, and A. S. Flø et.al. “Noninvasive photoluminescence imaging of silicon PV modules in daylight”. In: *Applied Physics Letters* 120 (24 June 2022). DOI: 10.1063/5.0097576.

[20] W. Mühleisen et al. “Scientific and economic comparison of outdoor characterisation methods for photovoltaic power plants”. In: *Renewable Energy* 134 (2019), pp. 321–329. ISSN: 0960-1481. DOI: 10.1016/j.renene.2018.11.044.

[21] W Mühleisen et al. “Scientific and economic comparison of outdoor characterisation methods for photovoltaic power plants”. In: *Renewable energy* 134 (2019), pp. 321–329.

[22] A.A. Yaroshevsky. "Abundances of chemical elements in the Earth's crust". In: *Geochemistry International* 44 (2006), pp. 48–55. DOI: 10.1134/S001670290601006X.

[23] A. Smets and K. Jäger et. al. *Solar Energy - The physics and engineering of photovoltaic conversion technologies and systems*. UIT Cambridge, 2016, p. 80.

[24] A. Smets and K. Jäger et. al. *Solar Energy - The physics and engineering of photovoltaic conversion technologies and systems*. UIT Cambridge, 2016, pp. 48–50.

[25] K. A. Dornelles and M. Roriz et. al. "Thermal Performance of White solar-Reflective Paints for Cool Roofs and the Influence in the Thermal Comfort and Building Energy Use in Hot Climates". In: *ISES Solar World Congress 2011* (Aug. 2011). DOI: 10.13140/RG.2.1.1745.5843.

[26] Y. Augarten et al. "*Luminescence Shunt Imaging: Qualitative and Quantitative Shunt Images Using Photoluminescence Imaging*". In: *24th European Photovoltaic Solar Energy Conference (EU PVSEC* (Sept. 2009).

[27] International Energy Agency, 2021. *Bifacial Photovoltaic Modules and Systems: Experience and Results from International Research and Pilot Applications 2021*. Accessed: 2023-11-03. 2021.

[28] P. G. Ellingsen and N. K. Reitan et. al. "*Hyperspectral analysis using the correlation between image and reference*". In: *Journal of Biomedical Optics* 18 (2 Jan. 2013), p. 3. DOI: 10.1117/1.JBO.18.2.020501.

[29] Deepshikha Acharya et al. "Application of adaptive Savitzky-Golay filter for EEG signal processing". In: *Perspectives in Science* 8 (2016). Recent Trends in Engineering and Material Sciences, pp. 677–679. ISSN: 2213-0209. DOI: 10.1016/j.pisc.2016.06.056.

[30] Hadi Kordestani and Chunwei Zhang. "Direct Use of the Savitzky-Golay Filter to Develop an Output-Only Trend Line-Based Damage Detection Method". In: *Sensors* 20.7 (2020). ISSN: 1424-8220. DOI: 10.3390/s20071983.

[31] *Photovoltaic devices - Part 13: Electroluminescence of photovoltaic modules*. TS 60904-13:2018(E). Rev. 10.0. International Electrotechnical Commission (IEC). 2018.

[32] Claire Mantel et al. “SNR Study of Outdoor Electroluminescence Images under High Sun Irradiation”. In: *2018 IEEE 7th World Conference on Photovoltaic Energy Conversion (WCPEC) (A Joint Conference of 45th IEEE PVSC, 28th PVSEC & 34th EU PVSEC)*. 2018, pp. 3285–3289. DOI: 10.1109/PVSC.2018.8548264.

[33] L. Koester et al. “Quality Assurance of the Photovoltaic Power Plants Installation Stage - a Complementary Strategy Based of Photoluminescence and Steady-State Thermography”. In: *38th European Photovoltaic Solar Energy Conference and Exhibition*. DOI: 10.4229/EUPVSEC20212021-5DO.2.2.

[34] *465W MBB Bifacial Mono PERC Half-cell Double Glass Module - JAM42D20 440-465/MB Series*. (Visited on 03/29/2023).

[35] *Owl 640 S*. (Visited on 03/29/2023).

[36] Qinbang Zhou et al. “An Automatic Surface Defect Inspection System for Automobiles Using Machine Vision Methods”. In: *Sensors* 19.3 (2019). ISSN: 1424-8220. DOI: 10.3390/s19030644.

[37] Yavuz Selim Balcioglu, Bulent Sezen, and Ceren Cubukcu Cerasi. “Solar Cell Busbars Surface Defect Detection Based on Deep Convolutional Neural Network”. In: *IEEE Latin America Transactions* 21.2 (2023), pp. 242–250. DOI: 10.1109/TLA.2023.10015216.

[38] M Köntges et al. “Quantifying the risk of power loss in PV modules due to micro cracks”. In: *25th European Photovoltaic Solar Energy Conference, Valencia, Spain*. 2010, pp. 3745–3752.

APPENDICES

A - IRRADIANCE

All irradiance values are given in Table A.1. The irradiances are the average value of the irradiances measured during the I-V curve sweep that is used in the analysis.

Table A.1: Average of measured irradiance

		Front [Wm-2]	**Rear [Wm-2]**
Direct Irradiance	PERC3	841	955
	PERC1	792	1016
Diffuse Irradiance	PERC3	45	73
	PERC1	53	40

B - CORRELATION COEFFICIENT

All correlation coefficients are summarised in Table B.1. Table B.1 summarises the PCC values calculated between the module/background pixel signal and the reference and smoothed reference signals.

Table B.1: Pearson Correlation Coefficients. All values are measurements from the south module imaged from the rear.

Irradiance	**Smoothing**	**Module**	**Background**
Direct	Yes	0.6	0.09
Direct	No	0.5	0.28
Diffuse	Yes	0.84	0.25
Diffuse	No	0.84	0.27

C - SIGNAL-TO-NOISE RATIO

Table C.1 summarises all calculated SNR values.

Table C.1: Signal-to-Noise Ratio

		Front	**Rear**
Direct	PERC3	4.6324	6.9452
Irradiance	PERC1	9.3682	4.5875
Diffuse	PERC3	7.4662	1.4933
Irradiance	PERC1	7.7209	7.8342

Norges miljø- og biovitenskapelige universitet
Noregs miljø- og biovitskapelege universitet
Norwegian University of Life Sciences

Postboks 5003
NO-1432 Ås
Norway